PKM2 diverts glycolytic flux in dependence on mitochondrial one-carbon cycle

Mohaned Benzarti[1,2], Anais Oudin[3], Elodie Viry[4], Ernesto Gargiulo[4], Maryse Schmoetten[5], Laura Neises[1], Coralie Pulido[6], Nadia I. Lorenz[7-10], Michael W. Ronellenfitsch[7-10], David Sumpton[11], Marc Warmoes[12], Christian Jaeger[12], Antoine Lesur[1], Etienne Moussay[4], Jerome Paggetti[4], Simone P. Niclou[2,3], Elisabeth Letellier[5], Johannes Meiser[1]*

[1]Cancer Metabolism Group, Department of Cancer Research, Luxembourg Institute of Health, Luxembourg, Luxembourg.

[2]Faculty of Science, Technology and Medicine, University of Luxembourg, 2 avenue de Université, Esch-sur-Alzette, Luxembourg.

[3]NORLUX Neuro-Oncology Laboratory, Department of Cancer Research, Luxembourg Institute of Health, Luxembourg, Luxembourg.

[4]Tumor Stroma Interactions, Department of Cancer Research, Luxembourg Institute of Health, Luxembourg, Luxembourg.

[5]Molecular Disease Mechanisms Group, Faculty of Science, Technology and Medicine, Department of Life Sciences and Medicine, University of Luxembourg, Esch-sur-Alzette, Luxembourg.

[6]Animal Facility, Department of Cancer Research, Luxembourg Institute of Health, Luxembourg, Luxembourg

[7]Dr. Senckenberg Institute of Neurooncology, University Hospital Frankfurt, Goethe University, Frankfurt am Main, Germany.

[8]German Cancer Consortium, Partner Site Frankfurt/Mainz, Frankfurt am Main, Germany;

[9]Frankfurt Cancer Institute (FCI), University Hospital Frankfurt, Goethe University, Frankfurt am Main, Germany.

[10]University Cancer Center Frankfurt (UCT), University Hospital Frankfurt, Goethe University, Frankfurt am Main, Germany.

[11]Cancer Research U.K. Beatson Institute, Switchback Rd, Bearsden, Glasgow G61 1BD, UK.

[12]Luxembourg Centre for Systems Biomedicine, University of Luxembourg, 6 Avenue du Swing, 4367 Esch-sur-Alzette, Luxembourg.

*Correspondence:

Email: johannes.meiser@lih.lu

Twitter: @JohannesMeiser

Abstract

Throughout the metastatic cascade, cancer cells are faced with harsh metabolic environments and nutritional stresses which apply selection pressure leaving only the most metabolically resilient cells to survive and form metastases. Metabolic characterisation of such cell populations *in vitro* is currently challenging. Using galactose as a tool compound to mimic glycolytic limitation within the tumour microenvironment of primary and secondary neoplastic sites, we were able to uncover metabolic flexibility and plasticity of cancer cells *in vitro*. In contrast to the established idea that high glycolytic flux and expression of dimeric PKM2 redirects carbons towards anabolic routes such as the pentose phosphate pathway and serine synthesis pathway (SSP), we have discovered by using stable-isotope tracing that also glycolytic limitation results in metabolic rewiring. Surprisingly, despite limited carbon availability and energetic stress, cells induce a near complete block of pyruvate kinase isozyme M2 (PKM2) to divert carbons towards SSP. Simultaneously, TCA cycle flux is sustained and oxygen consumption is increased, both supported by glutamine. Glutamine not only supports TCA cycle flux but also SSP via distinct mechanisms. Due to PKM2 block, malic enzyme exclusively supports TCA cycle flux while mitochondrial phosphoenolpyruvate carboxykinase supports SSP. Moreover, by using genetic modifications of different one-carbon (1C) cycle enzymes, we are able to reverse the PKM2 block suggesting a link between mitochondrial 1C cycle and pyruvate kinase. Thus we show that PKM2 inhibition acts as a branching point to direct glycolytic and glutamine carbons into distinct routes, overall supporting the metabolic plasticity and flexibility of cancer cells.

Introduction

Increased aerobic glycolysis has been identified as a characteristic of cancer cells almost 100 years ago and subsequently highlighted as a hallmark of cancer [1-3]. This is the phenomenon whereby cancer cells increase the fermentation of glucose to lactate even in the presence of oxygen, at the cost of releasing and thereby losing carbons as lactate [4]. Many theories have been suggested as to why cancer cells adopt such a biomass-wasteful and energy-inefficient phenotype with the majority of these theories circulating around the idea that mitochondria are unable to cope with very high rates of early glycolytic reactions that are driven by oncogenic signalling [5-10]. In these early steps of glycolysis, NAD^+ and ATP are consumed and need to be regenerated for glycolysis to continue. This regeneration of NAD^+ and ATP seems to be the decisive bottleneck where the cancer cell has to decide whether to ferment glucose or oxidise it fully in the TCA cycle [9, 11-13]. Indeed, two recent publications highlighted how aerobic glycolysis rates are decided based on NADH shuttle capacity and the regeneration of NAD^+ [12, 13]. Moreover, it was proposed that cells downregulate mitochondrial respiration to avoid ATP depletion when the mitochondria are unable to replenish ATP used in the early steps of glycolysis fast enough. Therefore, cells turn to ATP generation via lactate overflow to avoid an ATP crisis [4, 9, 11].

While it has been suggested that aerobic glycolysis is not the main driver of high proliferation rates [13], it remains undeniable that cancer cells engage high proliferative rates in favourable metabolic environments with ampleness of glucose being an example of such environments. Therefore, *in vitro* it might seem that cancer cells are fixed on aerobic glycolysis, while *in vivo* they actually display metabolic flexibility and plasticity [14]. This is to survive nutrient depleted and hostile metabolic environments within the local tumour microenvironment (TME) and along the metastatic cascade [15]. However, such metabolic flexibility is usually masked within *in vitro* studies due to the usage of synthetic media containing supraphysiological concentrations of various metabolites [16]. Aerobic glycolysis can be caused *in vitro* as cancer cells become reversibly addicted to glycolysis and repress their mitochondrial respiration in response to high glucose concentration in their respective media i.e. the Crabtree effect [11, 17].

One method to circumvent this glycolytic addiction and to unmask cancer cells metabolic flexibility *in vitro* is to substitute glucose for galactose. Galactose is metabolised via the Leloir pathway to produce glucose 6-phosphate (G6P), meaning that it can support glycolysis [18]. While glucose is converted into G6P in a one-step reaction by hexokinase (Km ~ 0.3 mM) [19, 20], galactose requires four biochemical reactions to continuously supply the cell with G6P with the initial reaction catalysed by galactosekinase having a Km value three times higher than hexokinase (galactokinase Km ~ 1 mM) [21]. This results in galactose providing a slow, yet continuous, supply of carbons, mimicking the TME where glucose is rapidly consumed but continuously being replenished via circulation [22, 23]. Therefore, we used galactose as an *in vitro* tool compound to mimic glycolytic limitation that occurs within the TME.

We have previously shown that cancer cells increase serine catabolism and formate overflow under glycolytic limitation even though biosynthetic demands were decreased [24], indicating a role for one-carbon (1C) cycle in bioenergetics and redox balance [25]. However, the functional advantage and the exact source of carbons for the increased serine catabolism and formate overflow under glycolytic limitation remains unknown. Moreover, it was previously highlighted that glutamine flux is rewired towards serine synthesis pathway (SSP) under glucose starvation via phosphoenolpyruvate carboxykinase 2 (PEPCK2) [26-29]. Both observations indicate that metabolic rewiring takes place towards SSP under glycolytic limitation, yet the exact mechanisms and metabolic advantages of this rewiring remain unclear. Building on these observations, we used stable-isotopic tracers and targeted metabolomics to study the metabolic fluxes of central carbon metabolism and the rewiring that takes place under glycolytic limitation. By using galactose to model glycolytic limitation, we observed a continued but decreased flux through glycolysis while oxygen consumption rates (OCR) were increased [24]. We were able to corroborate previous findings on the rewiring of glutamine metabolism towards SSP via PEPCK2. Surprisingly and despite increased OCR, galactose derived carbons did not enter the TCA cycle for mitochondrial oxidation, suggesting glutamine is the main substrate to support the TCA cycle in these conditions. This block on glycolytic carbons toward mitochondrial metabolism is facilitated by a strong pyruvate kinase isozyme M2 (PKM2) block, pinpointing PKM2 as the rewiring point in glycolysis under glycolytic limitation. Furthermore, we observed that the PKM2 block

106 redirects the limited glycolytic carbons toward SSP to support the survival and proliferation of cancer cells.
107 Finally, we observed an upregulation of the mitochondrial enzymes of 1C cycle where they cooperate to
108 support biosynthesis, bioenergetics and redox balance under glycolytic limitation. These findings reveal that
109 1C cycle is needed for the proliferation of cancer cells when faced with limited glycolytic supply, and blocking
110 lower glycolysis at PKM2 contributes to keeping the 1C cycle running in these conditions.

111 **Results**

112 **Cancer cells metabolize galactose and utilize it to support early glycolysis**

113 To ascertain that cancer cells are able to metabolize galactose (Gal), we used a fully labelled [U-^{13}C] Gal tracer
114 and compared the relative flux through the Leloir pathway (Fig. 1A) and early glycolysis to the fluxes
115 measured when a [U-^{13}C] glucose (Glc) tracer is used (Fig. 1B). The relative flux to UDP-glucose and UDP-
116 galactose was comparable between Glc and Gal tracing and even higher in the case of glucose 1-phosphate
117 in Gal (Fig. 1C-E). When looking at the glycolytic intermediate fructose 1,6-bisphosphate (F 1,6-BP), the ^{13}C
118 enrichment was comparable between both tracers suggesting a similar flux of Glc and Gal (Fig. 1F). Pentose
119 phosphate pathway (PPP) is usually highly enriched with ^{13}C within the first minutes of [U-^{13}C] Glc tracing
120 [30]. Consequently, we saw high enrichments using [U-^{13}C] Gal tracing in early PPP intermediate 6-
121 phosphogluconate M+6 (Fig. 1G). However, the ^{13}C enrichment in ribose 5-phosphate (R5P) and
122 sedoheptulose 7-phosphate (S7P) showed multiple labelled isotopologues indicating higher shunting of
123 carbons between PPP, early glycolysis and gluconeogenesis in Gal conditions (Fig. 1H, I). Overall, these data
124 demonstrate that cancer cells are able to utilise Gal to fuel early glycolysis and PPP intermediates through
125 the Leloir pathway.

126 **Glutamine and lactate maintain an upregulated oxidative TCA cycle function under glycolytic limitation**

127 To test the validity of using Gal as a tool compound to mimic glycolytic limitation, we sought to first measure
128 the contribution of other carbon sources to the TCA cycle that might support the elevated mitochondrial
129 metabolism under Gal as characterized by increased oxygen consumption rates (OCR) [24] (Fig. S1A). It was
130 previously shown that glutamine anaplerosis into the TCA cycle is increased under full glucose starvation [29,
131 31]. To test if this is also the case upon limited glycolytic flux (compared to full starvation), we first measured

132 glutamine consumption and observed generally no striking change in the consumption in multiple cancer cell
133 lines under glycolytic limitation (Fig. 2A). Subsequently, we performed [U-^{13}C] glutamine tracing in MDA-MB-
134 468, 4T1 and B16-F10 cell lines in Glc and Gal. Upon Gal, we noted an increased relative flux from glutamine
135 into the TCA cycle metabolites in all three cell lines (Fig. 2B-D), indicating that while the absolute consumption
136 was not changed, the usage of glutamine flux is altered. Under Glc, we observed that glutamine enrichment
137 in the TCA cycle metabolites decreased as we move away from glutamine. In contrast, the enrichment
138 remains unchanged under Gal (Fig. 2B-D), indicating that the TCA cycle is running with strongly reduced
139 carbon input from glycolysis. Yet, acetyl-CoA input is required to sustain glutamine oxidation through the
140 TCA cycle, hinting towards malic enzyme (ME) activity to sustain pyruvate levels under glycolytic limitation.
141 ME decarboxylates malate into pyruvate and indeed, we observed a substantial M+3 labelling of pyruvate
142 and lactate from [U-^{13}C] glutamine under glycolytic limitation (Fig. 2E and S1B). ME involvement is further
143 supported by an increase in citrate M+6 isotopologue enrichment from glutamine under Gal which suggests
144 increased usage of glutamine derived acetyl-CoA for citrate (Fig. 2F-H). Additionally, when looking at the ratio
145 of M+3 pyruvate/M+4 malate (ME flux), we observe a significant increase under glycolytic limitation (Fig. 2I)
146 [31]. These findings display the metabolic plasticity of cancer cells, as they are able to rewire their metabolism
147 to run the TCA cycle mainly on glutamine. However, we are still able to detect an unlabelled fraction in citrate
148 (Fig. 2F-H) which most likely results from fatty acid oxidation.
149 An additional carbon source that we might neglect with our *in vitro* setup is lactate whose build up is a
150 prominent feature of most solid tumours [32]. In fact, recent evidence from *in vivo* studies suggest that
151 lactate can be a major carbon source to the TCA cycle of cancer cells [33, 34]. To test if this feature can be
152 recapitulated in our *in vitro* model, we performed [U-^{13}C] lactate tracing at a concentration of 5 mM as this
153 was indicated as a physiological relevant concentration within the TME [22, 35]. Supported by the increase
154 in NAD^+/NADH ratio (Fig. 2J), we measured increased ^{13}C contribution to pyruvate and the TCA cycle under
155 glycolytic limitation from [U-^{13}C] lactate (Fig. 2K, 2L and S1C, S1D). Of note, the lactate derived carbon
156 contribution to the TCA cycle was mainly via PDH and not via pyruvate carboxylase (Fig S1E, S1F). In summary,
157 we conclude that glutamine and lactate can substitute for glucose to support and run lower glycolysis and

158 the TCA cycle. In the case of lactate, this is facilitated by the increased NAD^+/NADH ratio favouring lactate
159 oxidation. Other carbon sources might also contribute towards the TCA cycle, however, these contributions
160 are expected to be smaller in comparison to the sources highlighted in this study [33]. Finally, the sustained
161 PDH flux (Fig. S1E) under Gal suggests that a block upstream of PDH prevents glycolysis derived entry into
162 the TCA cycle.

163 **Glutamine metabolism is redirected towards SSP under glycolytic limitation via PEPCK2**

164 It has previously been shown that under full glucose starvation, gluconeogenesis enzyme PEPCK2 becomes
165 active and supports the biosynthesis of glycolytic intermediates [26-29, 36]. To test if this is also the case in
166 Gal and not only upon full hexose starvation, we monitored glutamine derived carbon contribution to
167 phosphoenolpyruvate (PEP) and 3-PG (Fig. S2A-B) and observed an active PEPCK flux also upon low glycolytic
168 flux. Furthermore, we observed that the ^{13}C enrichment was similar under serine/glycine (SG) starvation
169 conditions. Overall, we were able to confirm PEPCK activity in three different cancer cell lines with up to 30%
170 of the measured serine being fully labelled under SG starvation (Fig. 3A). Even with SG in the medium, the
171 glutamine flux to serine under Gal was comparable to the one from Glc (Fig. 3B). As serine is the major
172 substrate for 1C metabolism, we measured the flux from glutamine into vital downstream metabolites of 1C
173 metabolism. We observed ^{13}C enrichment in ATP (Fig. 3C), glutathione (GSH) (Fig. 3D) and formate (Fig. S2C).
174 Of note, the labelled fraction of ATP reached an astonishing 40-50% under SG starvation in all three cell lines
175 (Fig. 3C).

176 PEPCK catalyses the decarboxylation of oxaloacetate into PEP, therefore, we can measure its metabolic flux
177 by using aspartate as a surrogate for oxaloacetate as the tracer medium contains no aspartate [37]. Doing
178 so, we observed a clear increase in PEPCK flux under glycolytic limitation with and without SG (Fig. 3E).
179 Mitochondrial PEPCK (PEPCK2) has been identified as the major isoform present in most tumour tissues [26].
180 Here we observed that PEPCK2 protein expression was markedly increased under glycolytic limitation in all
181 the cell lines tested (Fig. S2D). Subsequently, we used two different genetic approaches to target PEPCK2;
182 we knocked down PEPCK2 in MDA-MB-468 cells using shRNA and knocked it out using CRISPR/Cas9 system
183 in 4T1 and B16-F10 cells (Fig. S2E, F). Overall, we were able to confirm PEPCK2 as the culprit for the ^{13}C

184 enrichment into serine from glutamine (Fig. 3F). More importantly, serine intracellular levels significantly
185 dropped in MDA-MB-468 and 4T1 but not in B16-F10, signifying the importance of the glutamine flux for the
186 serine pool while also highlighting varying cell line specific dependencies on PEPCK2 (Fig. 3G). Furthermore,
187 the labelling into ATP and GSH was significantly reduced in PEPCK2 KD and eliminated in the KOs (Fig. 3H, I),
188 while formate overflow was unchanged in the PEPCK2 KOs (Fig. S2G). Moreover, we observed a mild increase
189 in the labelling of TCA cycle intermediates and pyruvate from glutamine in PEPCK2 KD/KOs which most likely
190 is a result of the elimination of the flux through PEPCK (Fig. S2H, I). Despite the significance of the glutamine
191 flux into SSP, we noted no difference in proliferation of 4T1 PEPCK2KO under glycolytic limitation (Fig. 3J).
192 This indicates that 4T1 cells are able to compensate for the missing contribution into serine by either
193 increasing uptake of serine from the medium or increasing the flux from Gal under SG starvation (Fig. S2J).
194 Overall, by using Gal as a tool compound, we were able to see that glutamine metabolism is rewired in cancer
195 cells to run the TCA cycle independently and to support SSP via enhanced activity of PEPCK2 (Fig. 3K).
196 However, it remains unclear how PEPCK2 and ME fluxes are coordinated as these fluxes cannot be
197 disentangled by using [U-^{13}C] glutamine. Therefore, we opted to use [U-^{13}C] Gal as a tracer to clearly follow
198 the glycolytic flux into lower glycolysis and TCA cycle under glycolytic limitation.

199 **Cancer cells sustain carbon flux towards SSP under glycolytic limitation**

200 To study the relative fluxes of lower glycolysis under glycolytic limitation in more detail we used [U-^{13}C] Gal.
201 Across a panel of nine different cancer cell lines representing four different tumours (breast, colorectal,
202 glioblastoma and melanoma) we observed robust Gal metabolization through glycolysis and SSP (Fig. 4A-C).
203 Despite similar enrichment in F 1,6-BP (Fig. 1F), the relative flux of ^{13}C in Gal decreased towards late glycolytic
204 intermediates with especially pyruvate showing only about 10% of the ^{13}C enrichment observed under Glc,
205 which could be explained partly by the increased flux from [U-^{13}C] glutamine under Gal (Fig. 4B). In
206 comparison, cells appeared to keep about 25 – 50% of their relative flux towards serine under Gal (Fig. 4C).
207 To exclude that this effect is due to differences in the time needed to reach isotopic steady state [37], we
208 performed a time course experiment. We observed isotopic steady state conditions with both tracers at
209 around 24h and longer incubation times did not result in higher ^{13}C enrichment of pyruvate, suggesting that

210 the different labelling pattern in pyruvate is not a result of different flux rates but of an alteration of central
211 carbon metabolism upon Gal (Fig. S3A). Furthermore, different Gal concentrations also did not affect how
212 much [U-^{13}C] Gal enriched the pyruvate pool (Fig. S3A) nor did the usage of RPMI-1640 (Fig. S3B). Using
213 dialysed or normal FBS did not affect pyruvate enrichment as well (Fig. S3C). To test the [U-^{13}C] Gal
214 enrichment in a more physiological setting, we repeated the ^{13}C tracing in Plasmax medium [38] and observed
215 similar reduction in M+3 pyruvate isotopologue between Gal and Glc (Fig. S3D). To eliminate the possibility
216 of an inhibitory action of Gal, we mixed Glc and Gal in a 1:1 mix where the Glc added was ^{13}C. If Gal had a
217 direct inhibitory action on glycolysis we would expect to see a clear reduction of ^{13}C flux towards pyruvate,
218 however, we observed no difference in ^{13}C enrichment in glycolysis under such conditions (Fig. S3E). These
219 observations indicate that the reduced glycolytic ^{13}C flux is a result of the cells' response to the limited
220 availability of carbons under Gal.
221 To better visualise the differences between the relative flux towards lower glycolysis and SSP, we used 3-PG
222 (divergent point between SSP and lower glycolysis) M+3 isotopologue as a common denominator to
223 normalise the main labelled isotopologue of different metabolites (e.g. M+3 serine/M+3 3PG, M+3
224 pyruvate/M+3 3PG, M+2 citrate/M+3 3PG etc). The resulting ratios are presented as a fold change of the
225 same ratios under Glc (Fig. 4D, E). We found that in most cell lines the ratio for serine under Gal was
226 comparable or higher than under Glc, which indicates comparable or higher flux to SSP under glycolytic
227 limitation. In contrast, the ratio of M+3 pyruvate / M+3 3PG was strikingly lower under Gal than under Glc,
228 which indicates significantly less carbon flux towards pyruvate under Gal. Thus, we observed that cancer cells
229 re-wire their limited ^{13}C supply under Gal towards SSP resulting in SSP as the significantly favoured
230 destination compared to lower glycolysis. This phenotype was predominant in cell lines which doubled under
231 24h (fast-growing) (Fig. 4D, E). One exception was the murine breast cancer cell line 4T1, which is extremely
232 glycolytic and is very sensitive to Gal, indicating that this cell line may not be able to adapt to such an
233 environment (Fig. 4E). Furthermore, we took note of a similar observation of the rewiring when looking at
234 the intracellular levels of serine and pyruvate (Fig. 4F, G). Subsequently, we validated the re-wiring
235 phenotype when MDA-MB-468 were cultured in the physiological medium Plasmax (Fig. 4H). When ^{13}C-Glc

236 was mixed 1:1 with ^{12}C-Gal, we saw that there was no change in the ^{13}C flux ratios, showing again that Gal is
237 not inhibitory of glycolysis (Fig. 4I). However, when ^{13}C-Gal was mixed with ^{12}C-Glc we saw that the flux was
238 heavily favoured towards pyruvate and lactate and not to SSP (Fig. 4I). This indicates that under ample supply
239 of glycolytic carbons, ^{13}C flux from Gal is not rewired towards SSP.
240 Based on the observed rewiring, we checked the expression of SSP enzymes and observed a modest increase
241 in the protein expression of phosphoserine aminotransferase 1 (PSAT1) and phosphoserine phosphatase
242 (PSPH), while phosphoglycerate dehydrogenase (PHGDH) expression was mostly not elevated (Fig. S3F, S3G).
243 This indicates that the sustained flux through SSP is not a result of altered gene expression but rather a more
244 direct metabolic adaptation of enzyme activity. In summary, under glycolytic limitation, fast-growing cancer
245 cells (cell lines with doubling times <24 hours) re-wire their metabolism upon limited glycolytic flux towards
246 SSP at the cost of pyruvate oxidation.
247 **Glycolytic limitation inhibits glycolysis at PKM2**
248 Having identified a block at lower glycolysis and re-routing of glycolytic carbons towards SSP, we looked to
249 determine how cancer cells mechanistically undergo the proposed re-wiring. Since the re-wiring occurs
250 somewhere between 3-PG and pyruvate, we hypothesised that this might occur at pyruvate kinase which is
251 a known regulatory node of glycolysis [39] (Fig. 5A). This hypothesis is supported by the observation that
252 under Gal cancer cells excrete almost no lactate (Fig. S4A) and its intracellular levels drop significantly (Fig.
253 4F). This finding also explains why cancer cells are very vulnerable to adenine nucleotide translocator (ANT)
254 inhibition under glucose starvation [40] as in the absence of lactate production they would be highly relying
255 on mitochondrial ATP. Specifically, we have observed that PEP accumulates under Gal while pyruvate levels
256 drop dramatically (Fig. 5B-E), further supporting the hypothesis that the metabolic block occurs at the level
257 of pyruvate kinase. This is further substantiated by the observation that ^{13}C labelling in pyruvate is nearly
258 absent across all cell lines analyzed, while PEP remains significantly labelled (Fig. 5B-E). To confirm the
259 glycolytic block at PKM2, we used the PKM2 activator TEPP-46 [41] and repeated stable isotope tracing with
260 [U-^{13}C] Gal. The activation of PKM2 increased the ^{13}C flux towards citrate at the cost of serine synthesis (Fig.
261 5F). Furthermore, we observed a significant reduction of the labelling into serine from [U-^{13}C] glutamine

solidifying our model that the rewiring into SSP is supported by PKM2 inhibition (Fig. S4B). Finally, the activation of PKM2 and subsequent prevention of the rewiring towards SSP lead to a significant decrease in proliferation of MDA-MB-468 (Fig. 5G) and reduction in 3D growth using anchorage-independent conditions (Fig. S4C), concluding that maybe not the PEPCK2 flux but the inhibition of the PKM2 flux is important for survival, at least in our experimental setup (Fig. 3J, 5G). F 1,6-BP binds to PKM2 and induces the formation of the active tetramer form [42, 43]. Under Gal we saw that the intracellular levels of F 1,6-BP drop (Fig. S4D) which is known to lead to a reduction in PKM2 activity [42, 43]. However, what we observe with Gal is a complete block of the glycolytic flux at PKM2, indicating that factors other than the low levels of F 1,6-BP are contributing to this rewiring.

In summary, we provide so far evidence that when hexose availability for glycolysis is limited, the residual glycolytic carbon remains in upper glycolysis to support SSP. Meanwhile, glutamine and lactate compensate for carbon demand of the TCA cycle to support increased mitochondrial respiration. Moreover, we are able to increase the mechanistic granularity of the glutamine rewiring through ME and PEPCK by identifying the PKM2 block which means that ME flux (Gln --> Pyruvate) is exclusive to supporting the TCA cycle while PEPCK flux (Gln --> PEP) is exclusive to support SSP (Fig. 5H).

SSP is needed for proliferation and viability under glycolytic limitation

Next, we sought to investigate the functional advantage of the observed metabolic re-wiring towards SSP. We noted a weak correlation between the growth rate of cancer cells under Glc and to what extent Gal inhibited their proliferation (Fig. 6A). Based on that observation we studied the proliferative capacity of the MDA-MB-468 cell line upon treatment with a competitive inhibitor of PHGDH (the rate-limiting enzyme of SSP) BI-4916 [44] while under glycolytic limitation. We observed the lowest proliferative capacity of MDA-MB-468 cells when SSP was inhibited under glycolytic limitation (Fig. 6B). MDA-MB-468 cells grown in 3D using anchorage independent conditions with both normal and dialysed FBS also showed the significant growth reduction upon SSP inhibition and glycolytic limitation (Fig. 6C, D and S5A). We further confirmed these results in different cancer cell lines with similar results for two out of three cell lines tested (Fig. 6E). Lastly, we also analyzed the viability of different cancer cell lines in Gal treated with BI-4916 and compared

288 the fold-change apoptosis induction to Glc cultivation in different cell lines. We found an increased
289 percentage of apoptotic (Ann V^+) cells when PHGDH flux was blocked under glycolytic limitation (Fig. 6F). The
290 exception is here again the 4T1 cell line, a finding that matches the fact this was the only cell line not
291 showcasing the observed rewiring towards SSP under glycolytic limitation (Fig. 4E). Overall, it is evident that
292 sustained SSP exerts a pro-proliferative and anti-apoptotic role under glycolytic limitation.

293 **SSP flux is crucial to sustain mitochondrial formate production and to support all three metabolic pillars**

294 In addition to serine synthesis, we were interested to understand the functional relevance of sustained serine
295 availability. We sought to uncover the metabolic purpose of such rewiring, especially since 1C metabolism is
296 able to support all of the three metabolic pillars; biosynthesis, bioenergetics and redox balance [25] (Fig. 7A).
297 We analyzed the expression of the different enzymes of the 1C cycle and found that the mitochondrial
298 enzymes SHMT2 and MTHFD2 displayed increased mRNA expression under glycolytic limitation while the
299 expression of their cytoplasmic versions were mostly kept unchanged with MTHFD2 expression also
300 increased at the protein level (Fig. 7B-C). The product of the mitochondrial 1C cycle branch is the release of
301 the 1C unit as formate and we have previously shown that serine catabolism and formate overflow increase
302 upon Gal [24]. In corroboration, we performed formate measurements in a panel of cancer cell lines and
303 observed increased formate release under glycolytic limitation across the cell lines tested (Fig. 7D). Similar
304 to lactate overflow, formate overflow produces one ATP molecule per MTHFD1L reaction. In addition to ATP
305 production, formate overflow yields one NADH molecule via MTHFD2 [45]. The coupling of MTHFD2-derived
306 NADH to the electron transport chain (ETC) thereby contribute to mitochondrial ATP production and the
307 observed increase in OCR upon Gal (Fig. S1A)[24]. Meaning that the increased formate release can serve as
308 a crucial bioenergetic function by supporting mitochondrial ATP production under glycolytic limitation [24].
309 Furthermore, we have previously shown that under glycolytic limitation, AMPK is activated alongside the
310 increased formate release [24] which is an observation we could confirm in the glioblastoma cell line LN-229
311 (Fig. S6A). To test whether AMPK is responsible for the rewiring towards SSP and 1C cycle, we utilized LN-229
312 cells harbouring a genetic deletion of both alpha subunits of AMPK (Fig. S6B) [46]. We observed no difference
313 in the AMPKKO cells in terms of formate release (Fig. S6C) and ^{13}C flux rewiring (Fig. S6D), indicating that

314 AMPK activation and increased formate overflow are not in causal relation. Furthermore, knocking-out
315 MTHFD1L, the enzyme catalysing formate release, led to only a subtle decrease in growth of MDA-MB-468
316 cells in 2D and 3D anchorage-independent conditions under glycolytic limitation (Fig. S6E-G).
317 Having observed that the bioenergetic aspect of ATP production upon formate overflow might only partially
318 contribute to the functional implications during glycolytic restriction, we investigated potential additional
319 metabolic aspects of the 1C cycle that support redox balance and biosynthesis. The 1C unit donated by serine
320 can either be used for de novo purine and pyrimidine synthesis or can be oxidised to CO_2 via ALDH1L2 or
321 ALDH1L1 while generating NADPH in the latter reaction (Fig. 7A). NADPH provides the cell with reducing
322 equivalents required to counter reactive oxygen species (ROS). We explored both biosynthesis and redox
323 balance as potential sinks for the rewired ^{13}C flux. ALDH1L2 expression was markedly increased under
324 glycolytic limitations in different cancer cell lines while the expression of ALDH1L1 was unchanged at mRNA
325 level (Fig. 7B, 7E). This indicates that 1C metabolism is mostly involved in maintaining mitochondrial rather
326 than cytosolic redox state under glycolytic limitation. Moreover, when we cultivated the highly glycolytic
327 breast cancer cell line 4T1 (Fig. S4A) for 72h in Glc without medium change, we saw that the expression of
328 ALDH1L2 increased as Glc concentration became limited supporting the ALDH1L2 data we obtained using Gal
329 (Fig. 7F). Knocking out ALDH1L2 in MDA-MB-468 cells (Fig. S6H) resulted in mildly reduced proliferation under
330 glycolytic limitation in both 2D and 3D assays (Fig. 7G, H). Concurrent increased expression of ALDH1L2 and
331 increased formate overflow would together highlight the extent of increased carbon flux through SSP and 1C
332 cycle as despite the release of 1C as CO_2, formate overflow is still significantly increased.
333 PPP is a key regulator of biosynthesis and redox balance as it supplies the cells with R5P and NADPH [47]. The
334 cycling of carbons we observed (Fig. 1H, I) suggests that PPP is shifted towards maximising the production of
335 NADPH and R5P from the limited carbon supply under Gal. Due to this carbon cycling in PPP and subsequent
336 labelling of R5P, it is not possible to determine the contribution of 1C metabolism to nucleotide biosynthesis
337 by using [U-^{13}C] Glc and Gal tracers (Fig 7I and S6I-M). Therefore, we utilised [U-^{13}C] serine tracer and
338 observed that the flux from serine towards nucleotide biosynthesis is sustained under glycolytic limitation
339 (Fig. 7J). Overall, it can be concluded that the metabolic functions of the 1C metabolism are individually only

340 partially contributing to the functionality of cells under glycolytic limitation. Conclusively, this suggests the
341 idea that the flux through the mitochondrial 1C cycle might serve multiple metabolic purposes.
342 To test if mitochondrial 1C metabolism plays a combined role in controlling metabolic adaptation to glycolytic
343 limitation, we performed [U-^{13}C] Gal tracing in MTHFD1L and MTHFD2 KO cells (Fig. S6G) and found that the
344 we can detect an increase in labelling into TCA cycle upon loss of mitochondrial 1C cycle activity (Fig. 7K, L).
345 This can be seen in the decrease in ^{13}C flux to serine and glycine with concomitant increase of ^{13}C flux to
346 citrate (Fig. S6O, P). This effect was clearest in MTHFD1LKO and was similar to what we observed with PKM2
347 activation (Fig. 5F). These observations indicate that the mitochondrial 1C pathway contribute to the rewiring
348 of lower glycolysis.
349 Put together, it is apparent that the rewiring towards SSP and the plasticity of 1C metabolism under glycolytic
350 limitation serves all three metabolic pillars with sustained carbon flux from serine to purines and increased
351 ATP and NADPH generation. In particular, mitochondrial formate production needs to be increased, as an
352 increased fraction of formate is likely to be oxidized due to increased protein levels of ALDH1L2 while at the
353 same time formate overflow is also increased. Additionally, cytosolic formate is needed to support purine
354 and pyrimidine biosynthesis to sustain proliferation. Finally, we observed that loss of mitochondrial 1C
355 pathway activity results in ^{13}C carbon re-entry through PKM2 towards the TCA cycle.

356 ***In vivo* relevance of Gal to model glycolytic limitation**

357 The *in vitro* modelling of the metabolic environment that cancer cells face *in vivo* is extremely challenging
358 due to the heterogeneity of the tumour tissue and the varying metabolite composition of the TME. Using Gal
359 as a tool, we aimed to mimic glucose limitation as one important variable of the *in vivo* TME. To test the
360 physiological relevance of using Gal as a tool compound to study glycolytic limitation, we subcutaneously
361 injected B16-F10 cells into the flanks of C57BL/6 mice. We then allowed the tumours to grow for 16 and 9
362 days, thereby generating larger and smaller tumours, respectively, (Fig. 8A, B) and then we infused the mice
363 under anaesthesia with [U-^{13}C] Glc tracer for 2 hours. Next, we performed targeted metabolomics on pieces
364 of dissected tumour and compared the small tumours to the inside and the outside of the big tumours to
365 measure the gradient of metabolite levels between the outer layer and the core of the relatively big tumours.

We observed that glucose levels strikingly drop in the core of the big tumour compared to its outer layer (Fig. 8C). Meanwhile, other metabolites that can act as secondary carbon sources for tumours (lactate, glutamine and serine) were all present at similar levels between core and the outer layer (Fig. 8C). Moreover, when looking at the MIDs of 3-PG we can see that the ^{13}C enrichment is slightly higher on the outer layer than in the core (Fig. 8D). In tumours, when the ^{13}C fraction of pyruvate is normalised to the ^{13}C fraction of 3-PG, the ratio is equal to one when newly synthesised pyruvate is entirely generated by glycolysis [34]. The ratio is in contrast >1 when other ^{13}C sources outside of glycolysis, that are labelled elsewhere by [U-^{13}C] Glc and then supply the tumour from circulation, contribute to the pyruvate pool [34]. Comparing these ratios between the outer and inner layers of the B16-F10 tumours, we can see that the ratio is ~ 2.3 in the inner core and 1.5 in the outer layer (Fig. 8E). This indicates that the core is depleted of glucose in bigger tumours and cells within this core are relying more on other carbon sources due to altering their glycolytic usage i.e. metabolic flexibility. In contrast, serine ratios remain rather constant suggesting a switch of the glycolytic flux towards serine (Fig. 8E). Even though these data are not definitive proof, they hint towards similar rewiring as observed *in vitro* when culturing cells in Gal.

In a second *in vivo* model we performed the adoptive transfer of TCL1-355 into C57BL/6 mice as a model of chronic lymphocytic leukaemia (CLL) [48, 49]. In this model, leukemic B cells proliferate rapidly within the spleen which in theory should create areas depleted of glucose as within solid tumours which is what we are mimicking *in vitro* using Gal. Indeed, we have observed decreased glucose concentration in the spleens of CLL mice compared to healthy mice (Fig. 8F). Therefore, the CLL model can be employed as an *in vivo* model for glycolytic limitation. After the disease developed, mice were continuously infused via the tail vein with [U-^{13}C] Glc tracer for 2 hours. When comparing B cells from healthy spleens against CLL B cells from diseased spleens, we observed that CLL cells significantly increased their relative flux from glucose towards serine and glycine while showing a reduced flux towards citrate, indicating low pyruvate oxidation (Fig. 8G). This altered metabolic phenotype between normal and leukemic B cells *in vivo* is partly recapitulated *in vitro* by switching cancer cells from Glc to Gal. In summary, by using Gal we are able to capture relevant metabolic features of

391 tumour cells that occur in glucose depleted TME, specifically, the glycolytic rewiring towards serine to
392 support cancer cell metabolism.

393 **Discussion**

394 In the present study, we discover a novel rewiring of glycolytic flux towards SSP via a PKM2 block when the
395 supply of glycolytic carbons is inadequate as modelled with Gal as a tool compound to mimic glycolytic
396 limitation within the TME. In addition, we were able to corroborate previously described rewiring of
397 glutamine metabolism towards SSP under glucose starvation. However, by identifying the block of lower
398 glycolysis at PKM2, we were able to add another mechanistic layer that differentiates the glutamine flux
399 under glycolytic limitation to either exclusively support SSP via PEPCK2 or TCA cycle via ME (Fig. 5H). We
400 observed that both fluxes contribute to the survival and proliferation of several cancer cell lines and to supply
401 the 1C cycle with the necessary carbons to perform biosynthetic, bioenergetic and redox balance functions.
402 Cancer cells *in vitro* usually engage in aerobic glycolysis due to the ample availability of glucose. This does
403 not reflect glucose levels and cancer cell metabolism within the TME. A key metabolite that drives the
404 metabolic phenotype of cancer cells is glucose and its availability, which has been shown to be decreased in
405 the tumour interstitial fluid (TIF) when compared to plasma [22, 23]. TIF measurements represent the
406 average level of glucose across the area of the whole tumour. However, inside the tumour, areas do exist
407 where cells are even more deprived of glucose (Fig. 8C) and those cells withstanding such severe metabolic
408 stress (alongside other niche stresses) are the plastic cells that are capable of surviving the metastatic
409 cascade [15]. Uncovering the metabolic rewiring in these deprived cells hold therapeutic promise to target
410 cancer growth and metastasis [25].
411 By culturing cancer cells under glycolytic stress conditions, we were able to see their ability to use the same
412 carbon source for different functions (metabolic plasticity) upon the PKM2 block and rewiring of carbons
413 towards SSP. On the other hand, cancer cells also re-direct the glutamine flux towards SSP showcasing an
414 example of metabolic flexibility [14]. PEPCK2 is the main instigator of glutamine flux rewiring towards SSP. It
415 is intriguing that the mitochondrial isoform of PEPCK is involved under glycolytic limitations, as usually this
416 isoform is only involved when cytoplasmic NADH levels are not depleted [50]. However, under glycolytic

417 limitations, NAD/NADH ratio is increased and yet the cells still preferably engage PEPCK2 over cytoplasmic
418 PEPCK1 whose involvement would transfer mitochondrial NADH to the cytoplasm via malate oxidation [50].
419 This finding can be explained by the possibility that the gluconeogenesis pathway is activated mainly to
420 support SSP and therefore, cytoplasmic NADH is not required to reduce 1,3-bisphosphoglycerate into
421 glyceraldehyde 3-phosphate as per the conventional gluconeogenesis pathway. Furthermore, in our system
422 we did not observe a proliferative advantage in activating PEPCK2 under glycolytic limitation contrary to what
423 has previously been published on PEPCK2. One major difference in our setup compared to earlier studies
424 that could explain this observation is the usage of cell lines which have PHGDH amplification and are capable
425 of increasing their serine synthesis flux independent of PEPCK2.
426 The diversion of the glycolytic flux away from lower glycolysis and towards SSP offers many metabolic
427 advantages for the cell. For bioenergetics, SSP and subsequent 1C cycle generate two NADH and one ATP per
428 3-PG molecule, while lower glycolysis generates one ATP and consumes one NADH. Meaning if energy is the
429 main constraint for the cell under glycolytic limitation, it will benefit more from running SSP and the
430 subsequent serine catabolism and formate overflow [24]. Furthermore, the additional advantage of
431 sustaining the flux towards serine catabolism lies in its pathway flexibility. The fate of the 1C can be tailored
432 for the cell's need; full oxidisation of 1C via ALDH1L2 will generate NADPH, the MTHFD1L reaction will
433 generate ATP, or it can be incorporated in purines and dTMP in the cytosol [25]. Here we show that under
434 glycolytic limitation, the rewiring towards SSP and 1C cycle supports all the three different pillars of
435 metabolism, specifically the mitochondrial part of the 1C cycle (Fig. 7). In fact, we observe that even though
436 the cells increase the expression of ALDH1L2 and subsequently lose more carbon as CO_2, formate overflow
437 is still increased, highlighting the non-biosynthetic benefit of running the mitochondrial branch of the 1C
438 cycle under glycolytic limitation.
439 Cancer cells preferentially express PKM2 over other isozymes of pyruvate kinase as it provides them with the
440 metabolic flexibility to regulate the glycolytic flux, as PKM2 can be regulated via allosteric signals that shifts
441 its form between a high activity tetramer and a low activity dimer [42]. This allows cancer cells to rewire their
442 glycolytic flux towards biosynthetic pathways when needed by expressing the dimer form of PKM2 to

accommodate higher proliferative rates under high glycolytic flux [42]. In the present study, we observed a complete block PKM2 metabolic activity when the glycolytic flux is limited to rewire the limited carbon input towards SSP. Previous work has shown that serine acts as an allosteric activator of PKM2, while the lack of extracellular serine lead to an inhibition of PKM2 activity [51, 52]. Here we observed that when glucose is limited, even with serine/glycine available in the media, PKM2 glycolytic flux was inhibited. Indicating that even when serine was available for the cells, the lack of glycolytic carbons inhibited pyruvate kinase activity to rewire the glycolytic flux towards SSP. This observation highlights an intriguing difference between de novo serine synthesis flux and extracellular serine consumption and potentially could be explained by recent work that has shown that PHGDH functions beyond its catalytic activity within tumour cells and can allosterically regulate the function of phosphofructokinase [53]. Moreover, here we presented evidence that the removal of MTHFD2 or MTHFD1L was sufficient to partially re-establish PKM2 activity, meaning that mitochondrial 1C cycle is able to directly regulate PKM2 function alongside other regulators like F 1,6-BP. This would hint at a possible link between the PKM2 block and the increased formate overflow under glycolytic limitation. Entangling the direct cause of PKM2 block and the link with 1C cycle is the subject of ongoing work in our lab.

The findings presented here highlight the flexibility and plasticity of the biochemical network in tumour cells. These adaptive traits present a challenge in developing precision-medicine drugs that target the cells' metabolism. For such therapeutic strategies to be successful, context dependent understanding of environmental conditions and nutrient availability of the TME need to be considered alongside specific oncogenic driver mutations [54].

Acknowledgements:

We are grateful to Stephanie Kreis (University of Luxembourg) for providing us with B16-F10, A375, SKMeL28 cells, Clement Thomas (LIH, Luxembourg) for providing 4T1 and BT-20 cells and Lewis Cantley (Harvard Medical School) for providing MDA-MB-468 WT and MTHFD1LKO cells. We are grateful for all the technical and analytical support from the different metabolomics platforms towards the work presented here and in specific: Francois Bernardin from the metabolomics platform at LIH, Xiangyi Dong, Floriane Gavotto and Lucia

Gallucci from the LCSB metabolomics platform, Luxembourg. We are thankful for the support of the National Cytometry Platform (Quantitative Biology Unit, LIH) for support with flow cytometry measurements and analysis. Figures 1A, 1B, 3K, 5A, 5H, 7A and 8A were created with biorender.com.

M.B. is supported by the Fondation du Pélican de Mie et Pierre Hippert-Faber, under the aegis of the Fondation de Luxembourg. M.B. and J.M. are supported by the Luxembourg National Research Fund (FNR) ATTRACT program (A18/BM/11809970). J.M. is supported by FNR-PRIDE NEXTIMMUNE (PRIDE/11012546), FNR-PRIDE i2Tron (PRIDE19/14254520). E.L. is supported by the FNR-CORE program (C16/BM/11282028 and C20/BM/14591557), by a Proof of Concept FNR grant (PoC/18/12554295), a PRIDE17/11823097 and by i2Tron (PRIDE19/14254520). E.G., J.P., and E.M. are supported by grants from the FNR and Fondation Cancer (PRIDE15/10675146/CANBIO, C20/BM/14582635, and C20/BM/14592342). E.V. is supported by FNRS-Télévie (7.4509.20 and 7.4572.22).

Author's contribution:

M.B. and J.M. conceptualised and designed the study. M.B. performed all of the experiments. A.O., E.V., E.G., M.S., C.P., J.P., E.M., S.P.N. and E.L., assisted for the design and performing of the *in vivo* work. L.N., N.I.L. and M.W.R. aided in the generation of different KO cell lines used. D.S., M.W., C.J. and A.L. performed YSI, LC-MS, GC-MS and IC-MS measurements while M.B. performed the corresponding data analysis according to D.S., M.W., C.J., A.L., J.M., instructions. Original draft written by M.B. and J.M. Review and editing done by all authors.

Competing interest:

Authors of the presented study declare no competing interests.

Material and Methods:

<u>Chemicals</u>

Galactose, glucose, serine, glutamine and glycine were purchased from Sigma Aldrich and stock solutions were prepared in ^{MQ}water. BI-4916 and TEPP-46 were purchased from MedChemExpress and stocks were prepared in DMSO. BI-4916 was always used at a final concentration of 15µM while TEPP-46 was used at 100µM.

<u>Cell culture</u>

496 MDA-MB468, 4T1, MDA-MB-231, HCT116, LN-229 and B16-F10 were cultured in DMEM (Thermo Fisher
497 Scientific, 1443001) supplemented with 17.5 mM glucose, 2mM glutamine and 10% FBS. BT20 were cultured
498 in advanced DMEM/F12 (Thermo Fisher Scientific, 12634010) supplemented with 2 mM glutamine and 10%
499 FBS. A375 and SKMeL28 were cultured in RPMI 1640 (Thermo Fisher Scientific, 61870010) supplemented
500 with 10% FBS. All cells were maintained at 37°C and 5% CO_2 and routinely tested for mycoplasma
501 contamination. Serine/glycine starvation experiments were carried out using customised DMEM (Thermo
502 Fisher Scientific, lot No. GME11933004) without phenol red, glucose, serine, glycine, tryptophan, pyruvate
503 and glutamine with the missing ingredients added according to the concentrations present in full DMEM and
504 experimental setup. All experiments (except anchorage independent growth assays, see below) were seeded
505 on D-1 and cells were allowed to adhere and attach overnight. Medium was aspirated and experimental
506 medium plus treatment was added for the indicated time points in figures.
507 MDA-MB-468 WT and MTHFD1L-KO were received from Lewis Cantley lab, Weill Cornell Medical College,
508 USA [55]. STR profiling in our lab in 2021 authenticated MDA-MB-468. LN-229 WT and AMPK-dKO cells were
509 obtained from Michael Ronellenfitsch, Dr Senckenberg Institute of Neurooncology, University Hospital
510 Frankfurt, Goethe University and have been previously described in [46], B16-F10, A375 and SKMeL28 cells
511 were received from Stephanie Kreis lab, University of Luxembourg, Luxembourg. 4T1 and BT20 were received
512 from Clement Thomas lab, Luxembourg institute of Health, Luxembourg. MDA-MB-231 were obtained from
513 Alexei Vasquez lab, Beatson Institute of Cancer Research, UK. All cell lines were originally purchased from
514 ATCC.

515 **Lentiviral mediated knockdown of *PCK2***

516 The procedure followed was described in detail in [56]. For silencing *PCK2* gene in MDA-MB-468 cells, pGIPZ
517 shPCK2-2: ATTATTGGACAGTCTTTGT (V3LHS_410309) vector plasmid purchased from Horizon Discovery was
518 used.

519 **CRISPR/Cas9 KO of *Pck2, MTHFD2, ALDH1L2***

520 MDA-MB-468 cells harbouring deletion of MTHFD2 have been previously generated in [56]. To KO *Pck2* in
521 4T1 and B16-F10, we used the same procedure described in [56]; two different gRNAs were used: 1.
522 TATGCGTATTATGACCCGCC (Vector ID: VB211125-1122kdb, gRNA #654) to generate 4T1 clone A9 and B16-
523 F10 clone A5. 2. GCGGGTCATAATACGCATAC (Vector ID: VB211125-1123gfv, gRNA #653) to generate 4T1
524 clone B7 and B16-F10 clone A9. For *ALDH1L2* deletion in MDA-MB-468 cells the same procedure in [56] was
525 utilised with two different gRNAs: 1. GCAGAAGCCTACAGATCCGT (Vector ID: VB190719-1044jbf, gRNA #1529)
526 to generate MDA-MB-468 clone F11. 2. GCGCTCCGGCGCTTCTCCAC (Vector ID: VB190719-1054khg, gRNA #1st
527 Exon) to generate MDA-MB-468 clone D1.

528 **Animal experiments**

All experiments involving laboratory animals were conducted in a specific pathogen-free animal facility with the approval of the animal welfare structure of LIH and the Luxembourg Ministry for Agriculture, Viticulture and rural development under the references LUPA 2021/08 and LUPA 2021/22. Mice were treated in accordance with the European Directive 2010/63/EU. C57BL/6 mice were purchased from Janviers Labs (France).

TCL1-355 adoptive transfer

The TCL1-355 murine cell line was kindly provided by Dr Efremov [49]. A total of 2,000 TCL1-355 cells resuspended in DMEM without phenol red were injected intravenously (iv; 100 µL) in the tail vein of C57BL/6 mice. CLL progression was monitored by determining the percentage of $CD5^{+}CD19^{+}$ circulating CLL cells in the peripheral blood using flow cytometry. 14 days after iv injection, leukemic mice and age matched control mice were anaesthetised with 2.0 – 2.5% of isoflurane and continuously infused with [U-^{13}C] glucose (50% solution in 0.9% NaCl) for 2h at a constant rate of 1.8g/Kg/h via the tail vein. At the end of the infusion, mice were euthanized via cervical dislocation and blood, organs and cells collection was rapidly performed.

Blood sampling was performed before and after infusion. Plasma was collected after two successive centrifugations at 1000 RCF for 10 min. B cells were isolated from the spleen. Briefly, suspension of splenocytes was prepared using gentleMACS™ Dissociator (Miltenyi). Then, B cells isolation (negative sorting) was performed using MojoSort™ Mouse Pan B Cell Isolation Kit II (Miltenyi), according to manufacturer's instructions. Cells were counted prior to pelleting and snap freezing. Pieces of spleen were also snap frozen in liquid nitrogen for metabolomics.

B16-F10 subcutaneous model

A total of 250,000 B16-F10 cells resuspended in PBS were injected subcutaneously (100 µL) into the flank of C57BL/6 mice and tumours were allowed to grow for 16 days for one group and 9 days for the second group. At endpoint, both groups were infused with [U-^{13}C] glucose as described above. After infusion, mice were euthanized with cervical dislocation and blood was collected into heparin tubes to separate plasma. Plasma and tumour tissue were snap frozen in liquid nitrogen.

<u>Western blot</u>

KOs and KDs cell pellets were directly obtained from cell culture by pelleting cells at 350 RCF for 5 min followed by a PBS wash and then freezing at -20°C awaiting cell lysis. Probing protein expression after treatments: cells were cultured at 150,000 cells/well density in a 6-well plate on D-1. At time point of extraction, the plate was placed on ice, medium was aspirated and cells were washed in ice-cold PBS. Cell lysis buffer (150 mM NaCl, 1 mM EDTA, 50 mM Tris-HCl, 1% NP-40 with proteases and phosphatases inhibitors (Roche)) was added directly to the wells and cells were scraped and collected in pre-cooled Eppendorf tubes followed by sonification for 10 min. Lysates were spun at 16,000 RCF, 4°C for 10 minutes, the supernatant was collected in new tubes and the concentration of protein was determined with a Bradford

563 assay. 20 – 40 µg of total protein was loaded into 15-well or 12-well RunBlue 4-12% Bis-Tris gels (Westburg)
564 with the addition of 10mM DTT (Sigma Aldrich) and 4x NuPage LDS Sample buffer (Thermo Fisher Scientific)
565 and gels were run for 90 minutes at 120V. Protein bands were blotted onto nitrocellulose membrane for 2h
566 at 30 V. Membranes were blocked using 5% milk powder in TBS-0.1% Tween solution for 1h at RT.
567 Membranes were incubated in the corresponding primary antibody overnight at 4°C and for 1h at RT in
568 secondary antibodies. Detection of protein bands was done using Odyssey CLx Infrared Imaging system (LI-
569 COR). Image StudioLite software Vers.5.2 (LI-COR) was used for quantifications and analysis. Primary
570 antibodies used in this paper: AMPKα (Cell Signalling Technology, 5831S), p-AMPK^{Thr172} (Cell Signalling
571 Technology, 72335S), ACC (Cell Signalling Technology, 3676S), p-ACC^{Ser79} (Cell Signalling Technology, 11818S)
572 MTHFD2 (Cell Signalling Technology, ab151447), ALHD1L2 (Sigma Aldrich, HPA020549 and Proteintech,
573 21391-1-AP), β-Actin (Cell Signalling Technology, 3700), PSAT1 (Sigma Aldrich, HPA042924), PSPH (Sigma
574 Aldrich, HPA020376), PHGDH (Sigma Aldrich, HPA021241), PEPCK2 (Cell Signalling Technology, 6924S) and
575 MTHFD1L (Proteintech, 16113-1-AP). All antibodies were used at 1:1000 dilution unless stated otherwise.
576 Secondary antibodies: IRDye 680RD Goat Anti-Mouse IgG (H + L) (926-68070) and IRDye 800CW Donkey Anti-
577 Rabbit IgG (H + L) (926-32213) from LI-COR (used in a 1:10,000 dilution)..

578 **Flow cytometry analysis of Apoptosis**

579 250,000 cells (MDA-MB-468, B16-F10 and A375) or 200,000 cells (4T1) were seeded in 6-well plate, allowed
580 to attach overnight and treated as indicated for 48h. At endpoint, medium was collected, cells were washed
581 with PBS and PBS was collected followed by cell trypsinisation. Cells were pelleted and washed with ice-cold
582 PBS. Each sample was stained for 15 min on ice and in the dark with 50 µL AnnexinV staining solution (5%
583 AnnexinV-FITC antibody in AnnexinV binding buffer (10 mM HEPES pH 7.4, 140 mM NaCl, 2.5 mM $CaCl_2$, 0.1%
584 BSA in ^{MQ}water)). Directly prior to measurements, 450 µL of propidium iodide (PI) staining solution was added
585 (11.1 µg/ml in AnnexinV binding buffer). Measurements were done using NovoCyte Quanteon (Agilent) and
586 software NovoExpress (version 1.5.0). FlowJo version 10.6.2 was used for analysis.

587 **Proliferation assays**

588 Cells were seeded at a concentration of 25,000 cells/well in a 12-well plate or 12,500 cells/well in a 24-well
589 plate in triplicates. Separate triplicate wells were counted when treatment was added to set 0h count for
590 fold change calculations. Medium and treatment were replaced at 48h and 72h. At endpoint, cells were
591 trypsinised and viable cell count was obtained using Countess™ automated counter (Thermo Fisher). Growth
592 rate in Fig. 6A was calculated using the equation: [*ln*(final cell count/initial cell count)]/duration.

593 **Anchorage Independent 3D growth assays**

594 Cells were cultured in ultra-low attachment flask (Greiner) for a minimum of five days. Cells were collected
595 and spun at 100 RCF for 5 min and afterwards resuspended in Ca^{+2} and Mg^{+2} free PBS. 5,000 cells were seeded
596 in 96-well ultra-low attachment plates (S-Bio or facellitate) already in the experimental medium and the

597 plates were spun at 100 RCF for 10 minutes. 3D growth was determined using IncuCyte® S3 Live-Cell Analysis
598 system (Sartorius) over the indicated time periods.

599 **RNA extraction, cDNA synthesis and RT-qPCR**

600 300,000 cells were seeded in 6-well plate and treated for 24h as indictaed in the figures. RNA was extracted
601 directly from the plates using RNeasy Mini Kit (Qiagen, 74104). 2µg of RNA were used for cDNA synthesis
602 using High Capacity cDNA Reverse Transcription Kit (Thermo Fischer Scientific, 4368814). For qPCR, we used
603 Fast SYBR™ Green Master Mix (Thermo Fischer Scientific, 4368814) with 20 ng cDNA/sample in triplicates or
604 duplicates and the reaction was conducted at 95°C for 20 s followed with 40 cycles of 95°C for 1 s and 60°C
605 for 20 s. The QuantStudio 5 Real-Time PCR System was used (Applied Biosciences, ThermoFisher Scientific).
606 CT values were determined by QuantStudio Design and Analysis v1.5.1 software (Applied Biosciences,
607 ThermoFisher Scientific). Fold change of mRNA expression was determined using ddCt algorithm. Primers
608 used in this study are listed in Table S1.

Targeted gene	Species	Forward primer sequence	Reverse primer sequence
Psph	Mouse	AGATTTCCCAGGGATCCGGC	CAGTCCTCACTCAAGGCTCG
Psat1	Mouse	CCCAGCTGTGCGGAATGAGA	GAGCACACTGATGCCGAGTC
Phgdh	Mouse	CAGTGCAAGAAAGGTGTGCG	TTCTCGTGGTCCACTAAGGC
Shmt1	Mouse	TGCCCTCCCCATTTGAACAC	ATCTCTTTGCCAGTCTTGGGAT
Shmt2	Mouse	CTGCACAGTGGGGAGTCAAT	GTCAGTGCCAGGTTGAGCTT
Mthfd2	Mouse	CTGCGTTGGCTGTGCGGTT	CTGAGGTGTGGCCGCTTGT
Mthfd1	Mouse	CGTGGGTGGCAGACTAGCAA	TACCTGCTCCTGCATCCGAG
Aldh1l1	Mouse	TAGCAGGTGCCTTCCAACCT	CTTAAACACGGGCACGCCAT
Aldh1l2	Mouse	TTGACAGCCCAAAGCATGGC	CTGCCCAGAAAACAGAAAACCCA
Mthfd1l	Mouse	CTTTGGTGGGAACGATGAGCA	CCAGCCTTGACCGCATCTT
Gapdh	Mouse	CATCACTGCCACCCAGAAGACTG	ATGCCAGTGAGCTTCCCGTTCAG
Sdha	Mouse	CTTCGCTGGTGTGGATGTCA	GTGGGAATCCCACCCATGT
PSPH	Human	GACAGCACGGTCATCAGAGAAG	CGCTCTGTGAGAGCAGCTTTGA
PSAT1	Human	GGCTTGGTTCTGGAGTGGAT	ATGCCTCCCACAGACACGTA
PHGDH	Human	CTTACCAGTGCCTTCTCTCCAC	GCTTAGGCAGTTCCCAGCATTC
SHM1	Human	GAAGAAAATCTCTGCCACGTCC	GATCAGCTTCGGGTGGAAGAG
SHMT2	Human	GCCTCATTGACTACAACCAGCTG	ATGTCTGCCAGCAGGTGTGCTT
MTHFD1	Human	TTGGACAGGCTCCAACGGAGAA	AGAAGTGGTGAGAGCCAGGACA
MTHFD2	Human	CTCCTTGTTCAGTTGCCTCTTCC	CTGATCCAAACACATTCGTCCTAC
MTHFD1L	Human	CGCACACCTGAATGTCAACTCC	CGTGGATGTCTCCAGTCAAGTG

ALDH1L2	Human	CTTCTCCACTGGCCGGGTTTAT	CTGGAACTGTGAACACCCCT
GAPDH	Human	CATGAGAAGTATGACAACAGCCT	AGTCCTTCCACGATACCAAAGT
ACTINβ	Human	CACCCTGAAGTACCCCATCG	GCTGGGGTGTTGAAGGTCTC

Supplementary Table 1. List of primers used in this study and their sequences.

Metabolomics

Stable Isotope Tracing and Metabolite Extraction

- ***In vitro* tracing and metabolite extraction:**

Stable isotope tracing experiments with [U-^{13}C] glucose, [U-^{13}C] galactose, [U-^{13}C] glutamine, [U-^{13}C] serine (Cambridge Isotope Laboratories, CLM-1396, CLM-1570, CLM-1822 and CLM-1574 respectively) and [U-^{13}C] lactate (Sigma Aldrich, 485926) were performed in DMEM (Thermo Fisher Scientific, 1443001), RPMI 1640 for SILAC (Thermo Fisher Scientific, 88365), Advanced DMEM/F12 for SILAC (Thermo Fisher Scientific, A2494301) or customised DMEM (Thermo Fisher Scientific, lot No. GME11933004) depending on the cell lines used. These tracer mediums were supplemented with the missing metabolites according to the experimental setup to mimic the original formula of DMEM, RPMI 1640 or advanced DMEM/F12. For sodium [U-^{13}C] lactate 5 mM final concentration was used. For glucose and galactose tracing 10% normal FBS was used while for the rest we used 10% dialysed FBS. Experimental set-up and extraction of metabolites for GC-MS analysis was done as described in [56]. Metabolite extraction for LC-MS was done as described in [24]. Metabolite extraction for IC-MS was identical to LC-MS.

- ***In vivo* metabolite extraction**

Metabolite extraction from tumours, spleen and plasma was performed as detailed in [24]. The absolute quantification of glucose in plasma and spleen was performed using standard addition method. In brief, known concentrations of glucose were added serially to metabolite extracts of each sample. After measurements, a calibration curve was used to determine the concentration of glucose in the original samples by determining the x-axis intercept.

For B cells separated from the spleen, cells were washed with ice-cold PBS and subsequently 40 µL/one million cells extraction buffer [acetonitrile/$^{MQ}H_2O$/methanol (ratio, 3:2:5); liquid chromatography–MS (LC-MS) grade solvents)] was added to each cell pellet. Cells were mixed for 10 min on a thermomixer at 4°C at maximum speed, and then the tubes were centrifuged for 10 min at 16,100 RCF at 4°C. 50 µL of the supernatant was collected and transferred to an already-cooled LC-MS glass vial with inserts and stored at -80°C until measurement.

YSI measurements and medium exchange rates:

Medium samples were filtered (PVDF, 0.22 µm) prior measurement to remove particulates.

Absolute quantitative values for lactic acid and glutamine were acquired using a YSI 2950D Biochemistry Analyzer (Kreienbaum KWM). The instrument was calibrated and prepared according to the manufacturers' instruction. For a precise and reliable quantification, external concentration curves of each target compound were prepared and measured in triplicates. Absolute uptake and release rates were calculated as described in [24].

GC-MS measurements

- Formate measurements

Formate was derivatized to benzyl formate from the collected medium samples using the MCF protocol described in [24]. GC-MS analysis was performed using an Agilent 7890 A GC coupled to an Agilent 5975 C inert XL Mass Selective Detector (Agilent Technologies). A sample volume of 1 µL was injected into a Split/Splitless inlet, operating in split mode (20:1) at 280 °C. The gas chromatograph was equipped with a 30 m (I.D. 250 µm, film 0.25 µm) ZB-5MSplus capillary column (Phenomenex, 7HG-G030-11-GGA) plus 5 m GUARDIAN in front of the analytical column. Helium was used as carrier gas with a constant flow rate of 1.4 ml/min. GC oven temperature was held at 90 °C for 1 min and increased to 115 °C at 10 °C/min followed by 20 °C/min to 160 °C and a post run time of 4.25 min at 325 °C. Total run time was 10 min. Transfer line temperature was set to 280 °C. Mass selective detector (MSD) was operating under electron ionization at 70 eV. MS source was held at 230 °C and the quadrupole at 150 °C. For precise quantification, measurements were performed in selected ion monitoring mode. Target ions (m/z) and dwell times are listed below in Table S2. GC-MS chromatograms were processed using Agilent MassHunter Quantitative Analysis for GC-MS, Version B.08.00. Natural isotope correction and analysis of formate release rates was done as previously described in [24].

Derivative (Metabolite)	Quant-Ion (m/z)	Dwell Time (ms)
Benzyl Formate M_0	136.1	40
Benzyl Formate M_1	137.1	40
IS-Benzyl Formate (^{13}C,D) M_0	138.1	40
IS-Benzyl Formate (^{13}C,D) M_1	139.1	40
IS-Benzyl Formate(^{13}C,D) M_2	140.1	40

Supplementary Table 2. Dwell times and quantification ions for the derivatized formate.

- Intracellular metabolites measurements (Fig. S3A, C)

First, dried polar extracts were derivatized for 90 min at 55 °C with 20 µl of methoxyamine (c = 20 mg/ml) in pyridine under continuous shaking and subsequently for 60 min at 55 °C with additional 20 µl of MTBSTFA w/ 1% TBDMCS. GC-MS analysis was performed using an Agilent 7890B GC coupled to an Agilent 5977 A Mass Selective Detector (Agilent Technologies). A sample volume of 1 µl was injected into a Split/Splitless inlet, operating in splitless mode at 270 °C. Gas chromatograph was equipped with a 30 m (I.D. 250 µm, film

667 0.25 µm) ZB-35MS capillary column with 5 m guard column (Phenomenex). Helium was used as carrier gas
668 with a constant flow rate of 1.2 ml/min. GC oven temperature was held at 100°C for 2 min and increased to
669 300°C at 10°C/min and held for 4 min. Total run time was 26 min. Transfer line temperature was set to 280°C.
670 Mass selective detector (MSD) was operating under electron ionization at 70 eV. MS source was held at 230°C
671 and the quadrupole at 150 °C. For precise quantification of the MID, measurements were performed in
672 selected ion monitoring mode. The derivative measured here was pyruvic acid 1MeOX 1TBDMS with target
673 ions 174.0 – 180.1 [M-57 fragment] and dwell times of 15 ms. The MetaboliteDetector software package
674 (Version 3.220180913) was used for mass spectrometric data post processing, quantification, MID
675 calculations, correction of natural isotope abundance, and determinations of fractional carbon contributions
676 [57].
677 **IC-MS measurements** (Fig. 1C-I, Fig. S4D and S6I-K)
678 For the IC-MS measurements, polar extracts were analyzed as previously described [58] with the following
679 adjustments. 50-75% of the total polar extract was dried overnight under vacuum. Dried polar metabolite
680 pellets were reconstituted in 25 µl of water (Milli-Q Advantage A10) of which 20 µl was injected. For the ICMS
681 system, we interfaced a Dionex ICS-6000+ ion chromatograph coupled with a QExactive high resolution mass
682 spectrometer (Thermo Fisher Scientific). The guard, column, gradient settings, and suppressor type remained
683 unchanged [58]. The electrospray ionization (ESI) was set as follows: spray voltage of 2.500 kV, auxiliary gas
684 temperature of 420 °C, seep gas flow rate of 0, auxiliary gas flow rate of 15 units, and sheath gas flow rate of
685 50 units. The settings for acquisition of MS1 data were: m/z scan range of 80-750, resolution of 17500 at 200
686 m/z, automatic gain control (AGC) target of 1e6, and maximum injection time of 100 milliseconds. Data were
687 acquired using two micro-scans.
688 **LC-MS Measurements**
689 Metabolite analyses were performed using a Vanquish Flex LC coupled to a Q Exactive HF mass spectrometer
690 (Thermo Scientific). Chromatography was carried out with a SeQuant ZIC-pHILIC 5 µm particles column (150
691 x 2.1 mm) protected by SeQuant ZIC-pHILIC Guard (20 x 2.1 mm) pre-column. Column temperature was
692 maintained at 45°C. The flow rate was set to 0.2 ml/min and the mobile phases consisted of 20 mmol/L
693 ammonium carbonate in water, pH 9.2 (Eluent A) and Acetonitrile (Eluent B). The gradient was: 0 min, 80%
694 B; 2 min, 80% B; 17 min, 20% B; 18 min 20% B; 19 min 80% B; 20 min 80% B (0.4ml/min); 24 min 80% B
695 (0.4ml/min); 24.5 min 80% B. The injection volume was 5 µL. All MS experiments were performed using
696 electrospray ionization with polarity switching enabled . The source parameters were applied as follows:
697 sheath gas flow rate, 25; aux gas flow rate, 15; sweep gas flow rate, 0; spray voltage, 4.5 kV (+) / 3.5 kV (-);
698 capillary temperature, 325°C; S-lense RF level, 50; aux gas heater temperature, 50°C. The Orbitrap mass
699 analyzer was operated at a resolving power of 30,000 at 200 m/z in full-scan mode (scan range: *m/z* 75…1000;
700 automatic gain control target: 1e6; maximum injection time: 250 ms).

Data from IC-MS and LC-MS measurements were acquired with Thermo Xcalibur software (Version 4.3.73.11) and analyzed with TraceFinder (Version 4.1). Natural isotope subtraction and subsequent analysis were performed as previously described using in-house scripts [24].

Oxygen consumption rate measurements

10,000 cells (MDA-MB-468, 4T1 and MDA-MB-231) or 20,000 cells (HCT116) were seeded into 96-seahorse microplate (Agilent) on D-1. After attachment, glucose and galactose medium were added and cells were incubated for 24h. Basal OCR was measured using XF96 Extracellular Flux Analyzer (Seahorse bioscience, Agilent) following the manufacturer's protocol, Wave 2.6.0 software was used for analysis. OCR was normalised by the protein concentration of the corresponding wells following the protocol described in[59] and using a Bradford assay.

Statistics

Unless stated otherwise, unpaired two-tailed student's t-test with Welch's correction was used throughout the presented study as statistical tests were always performed between two groups. GraphPad PRISM (9.5.0) was used to calculate the *p* value. In the present study, *in vitro n* is defined as one independent experiment with at least two replicate wells (except for protein lysates and RNA samples where single wells were used). For *in vivo* experiments, *n* is defined as a sample from one mouse.

Figure 1

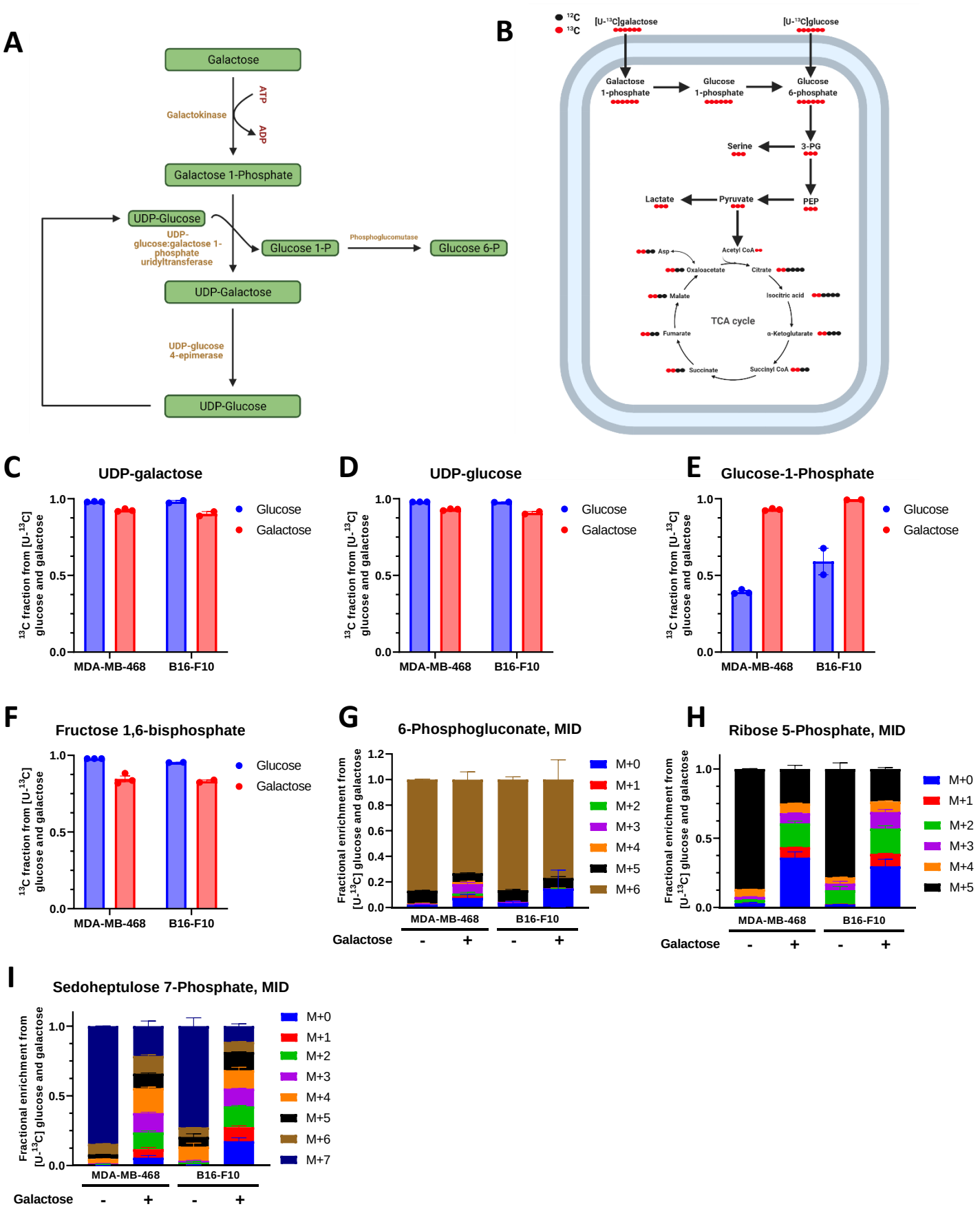
A
Galactose
Galactokinase
ATP
ADP
Galactose 1-Phosphate
UDP-Glucose
UDP-glucose:galactose 1-phosphate uridyltransferase
Glucose 1-P
Phosphoglucomutase
Glucose 6-P
UDP-Galactose
UDP-glucose 4-epimerase
UDP-Glucose
B
^{12}C
^{13}C
[U-^{13}C]galactose
[U-^{13}C]glucose
Galactose 1-phosphate
Glucose 1-phosphate
Glucose 6-phosphate
Serine
3-PG
Lactate
Pyruvate
PEP
Acetyl CoA
Asp
Oxaloacetate
Citrate
Malate
Isocitric acid
TCA cycle
Fumarate
α-Ketoglutarate
Succinate
Succinyl CoA
C
UDP-galactose
D
UDP-glucose
E
Glucose-1-Phosphate
^{13}C fraction from [U-^{13}C] glucose and galactose
Glucose
Galactose
MDA-MB-468
B16-F10
F
Fructose 1,6-bisphosphate
G
6-Phosphogluconate, MID
H
Ribose 5-Phosphate, MID
Fractional enrichment from [U-^{13}C] glucose and galactose
M+0
M+1
M+2
M+3
M+4
M+5
M+6
Galactose
I
Sedoheptulose 7-Phosphate, MID
M+7

Figure 1. Cancer cells metabolize galactose and utilize it to support early glycolysis. A Schematic representation of Leloir pathway for galactose metabolism. **B** Schematic representation of the expected labelling pattern of simplified central carbon metabolism when using [U-^{13}C] glucose and [U-^{13}C] galactose tracer. **C-F** ^{13}C fraction from [U-^{13}C] glucose and [U-^{13}C] galactose into UDP-galactose **(C)**, UDP-glucose **(D)**, glucose 1-phosphate **(E)** and fructose 1,6-bisphosphate **(F)** after 24h incubation. (**C-F**) Each dot represents an independent experiment averaged from 3 different replicate wells. **G-I** Fractional enrichment in 6-phosphogluconate **(G)**, ribose 5-phosphate **(H)** and sedoheptulose 7-phosphate **(I)** from [U-^{13}C] glucose and [U-^{13}C] galactose after 24h incubation. Data shown is mean±SEM of 3 (MDA-MB-468) or 2 (B16-F10) independent experiments each being the average of 3 different replicate wells.

Figure 2

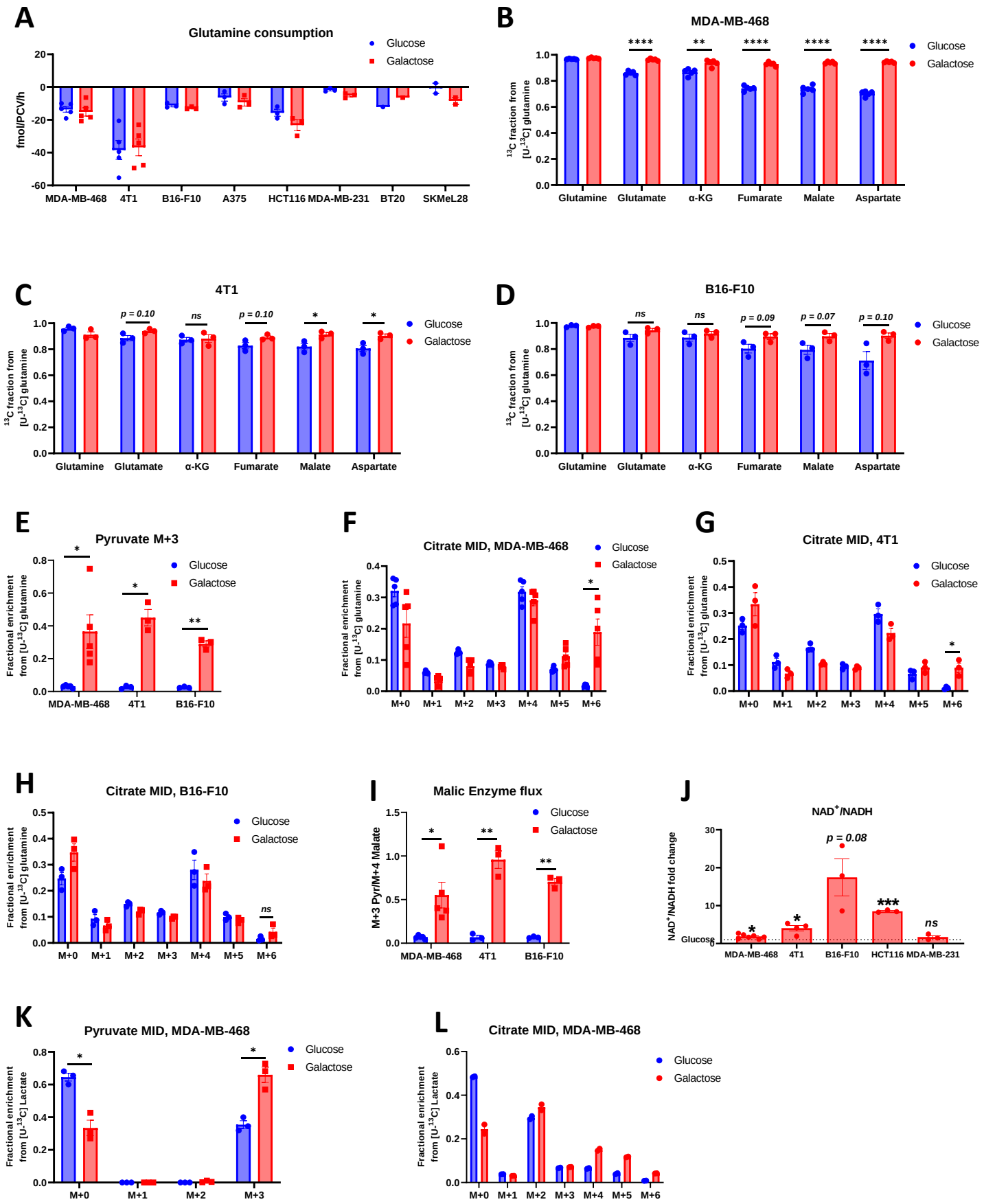
A
Glutamine consumption
Glucose
Galactose
fmol/PCV/h
MDA-MB-468
4T1
B16-F10
A375
HCT116
MDA-MB-231
BT20
SKMeL28
B
MDA-MB-468
^{13}C fraction from [U-^{13}C] glutamine
Glutamine
Glutamate
α-KG
Fumarate
Malate
Aspartate
C
4T1
p = 0.10
ns
p = 0.10
D
B16-F10
ns
ns
p = 0.09
p = 0.07
p = 0.10
E
Pyruvate M+3
Fractional enrichment from [U-^{13}C] glutamine
F
Citrate MID, MDA-MB-468
G
Citrate MID, 4T1
H
Citrate MID, B16-F10
I
Malic Enzyme flux
M+3 Pyr/M+4 Malate
J
NAD$^+$/NADH
p = 0.08
NAD$^+$/NADH fold change
Glucose
K
Pyruvate MID, MDA-MB-468
Fractional enrichment from [U-^{13}C] Lactate
L
Citrate MID, MDA-MB-468
M+0
M+1
M+2
M+3
M+4
M+5
M+6

Figure 2. Glutamine and lactate maintain upregulated oxidative TCA cycle function in reliance on malic enzyme (ME). **A** Absolute quantification of glutamine consumption from multiple cancer cell lines after 24h incubation with either glucose or galactose medium. **B-D** ^{13}C fraction in TCA cycle metabolites from [U-^{13}C] glutamine after 24h incubation with either glucose or galactose medium in MDA-MB-468 **(B)**, 4T1 **(C)** and B16-F10 **(D)**. **E** Fractional enrichment in M+3 pyruvate from [U-^{13}C] glutamine after 24h incubation with either glucose or galactose medium in MDA-MB-468, 4T1 and B16-F10. **F-H** Fractional enrichment in citrate from [U-^{13}C] glutamine after 24h incubation with either glucose or galactose medium in MDA-MB-468 **(F)**, 4T1 **(G)** and B16-F10 **(H)**. **I** Malic enzyme flux ratio calculated as M+3 pyruvate/M+4 malate isotopologues from [U-^{13}C] glutamine after 24h incubation with either glucose or galactose medium in MDA-MB-468, 4T1 and B16-F10. **J** NAD^+/NADH ratio measured with LC-MS in the indicated cancer cell lines after 24h incubation with galactose and normalised to the same ratio with 24h incubation with glucose medium. **K-L** Fractional enrichment in pyruvate **(K)** and citrate **(L)** from 5mM [U-^{13}C] sodium lactate after 24h incubation with either glucose or galactose medium in MDA-MB-468. (**A-L**) Each dot represents an independent experiment averaged from 3 different replicate wells unless stated otherwise. (**A-L**) Mean±SEM, * $p<0.05$, ** $p<0.01$, *** $p<0.001$, **** $p<0.0001$, ns $p>0.1$. *P* value is calculated by Student's t-test, two-tailed, unpaired with Welch's correction unless stated otherwise.

Figure 3

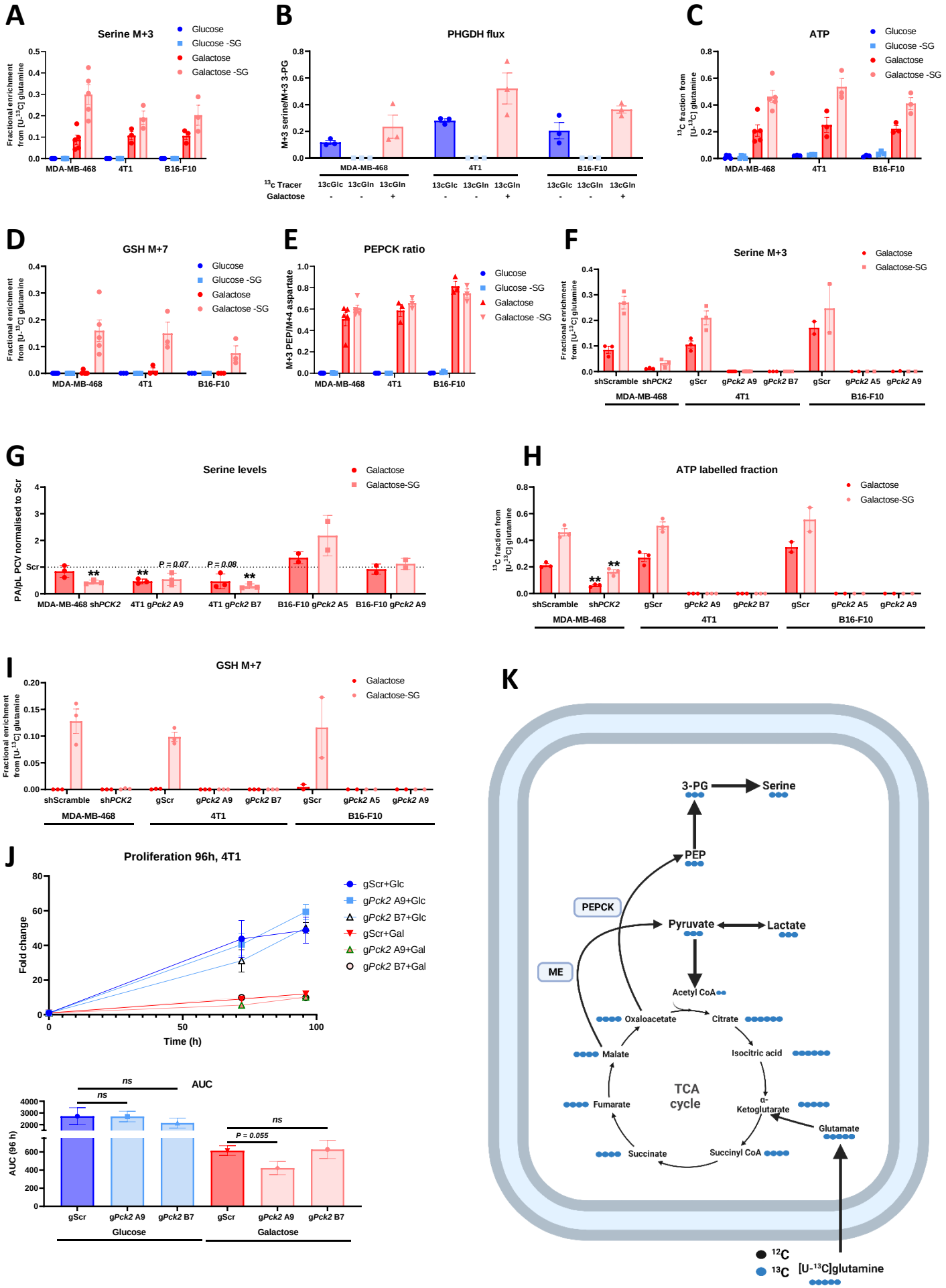
A
Serine M+3
Glucose
Glucose -SG
Galactose
Galactose -SG
Fractional enrichment from [U-13C] glutamine
MDA-MB-468
4T1
B16-F10
B
PHGDH flux
M+3 serine/M+3 3-PG
13C Tracer
Galactose
13cGlc
13cGln
C
ATP
13C fraction from [U-13C] glutamine
D
GSH M+7
E
PEPCK ratio
M+3 PEP/M+4 aspartate
F
Serine M+3
Galactose
Galactose-SG
shScramble
shPCK2
gScr
gPck2 A9
gPck2 B7
gPck2 A5
G
Serine levels
PA/pL PCV normalised to Scr
P = 0.07
P = 0.08
H
ATP labelled fraction
I
GSH M+7
J
Proliferation 96h, 4T1
Fold change
Time (h)
gScr+Glc
gPck2 A9+Glc
gPck2 B7+Glc
gScr+Gal
gPck2 A9+Gal
gPck2 B7+Gal
AUC
AUC (96 h)
ns
P = 0.055
Glucose
Galactose
K
3-PG
Serine
PEP
PEPCK
Pyruvate
Lactate
ME
Acetyl CoA
Oxaloacetate
Citrate
Malate
Isocitric acid
TCA cycle
Fumarate
α-Ketoglutarate
Glutamate
Succinate
Succinyl CoA
12C
13C
[U-13C]glutamine

744 **Figure 3. Glutamine metabolism is redirected towards SSP under glycolytic limitation via PEPCK. A** Fractional
745 enrichment in M+3 serine from [U-^{13}C] glutamine after 24h incubation with either glucose ± serine and glycine (SG) or
746 galactose ± SG medium in MDA-MB-468, 4T1 and B16-F10. **B** Phosphoglycerate dehydrogenase (PHGDH) enzyme flux
747 ratio calculated as M+3 serine/M+3 3-PG isotopologues from [U-^{13}C] glucose or glutamine (either with glucose or
748 galactose medium) after 24h incubation in MDA-MB-468, 4T1 and B16-F10. **C** ^{13}C fraction in ATP from [U-^{13}C] glutamine
749 after 24h incubation with either glucose ± SG or galactose ± SG medium in MDA-MB-468, 4T1 and B16-F10. **D** Fractional
750 enrichment in M+7 glutathione (GSH) from [U-^{13}C] glutamine after 24h incubation with either glucose ± SG or galactose
751 ± SG medium in MDA-MB-468, 4T1 and B16-F10. **E** Phosphoenolpyruvate carboxykinase (PEPCK) enzyme flux ratio
752 calculated as M+3 PEP/M+4 aspartate isotopologues from [U-^{13}C] glutamine after 24h incubation with either glucose ±
753 SG or galactose ± SG medium in MDA-MB-468, 4T1 and B16-F10. **F** Fractional enrichment in M+3 serine from [U-^{13}C]
754 glutamine after 24h incubation with either glucose ± SG or galactose ± SG medium in MDA-MB-468 shScramble and
755 sh*PCK2* cells, 4T1 and B16-F10 gScramble and g*Pck2* cells. **G** Peak areas (PA) of intracellular serine in PEPCK2 KD/KOs
756 normalised to packed cell volume (PCV) in picolitres (pL) and presented as fold change to the levels in scramble cells.
757 Data shown is for the levels measured in galactose ± SG medium. **H** ^{13}C fraction in ATP from [U-^{13}C] glutamine after 24h
758 incubation with galactose ± SG medium and the comparison between scramble and PEPCK2 KD/KOs cells. **I** Fractional
759 enrichment in M+7 glutathione (GSH) from [U-^{13}C] glutamine after 24h incubation with galactose ± SG medium and the
760 comparison between scramble and PEPCK2 KD/KOs cells. **J** 2D proliferation curve of 4T1 gScramble and g*Pck2* cells with
761 either glucose or galactose, with the corresponding area under the curve (AUC). 72h timepoint includes 3 independent
762 experiments while 96h includes 4 independent experiments (from at least 3 different replicate wells for each
763 independent experiment). (**A-J**) Each dot represents an independent experiment averaged from 3 different replicate
764 wells unless stated otherwise. (**A-J**) Mean±SEM, * $p<0.05$, ** $p<0.01$, *** $p<0.001$, **** $p<0.0001$, ns $p>0.1$. *P* value is
765 calculated by Student's t-test, two-tailed, unpaired with Welch's correction unless stated otherwise. **K** Schematic
766 representation of the rewiring of glutamine metabolism that take place under glycolytic limitation.
767

Figure 4

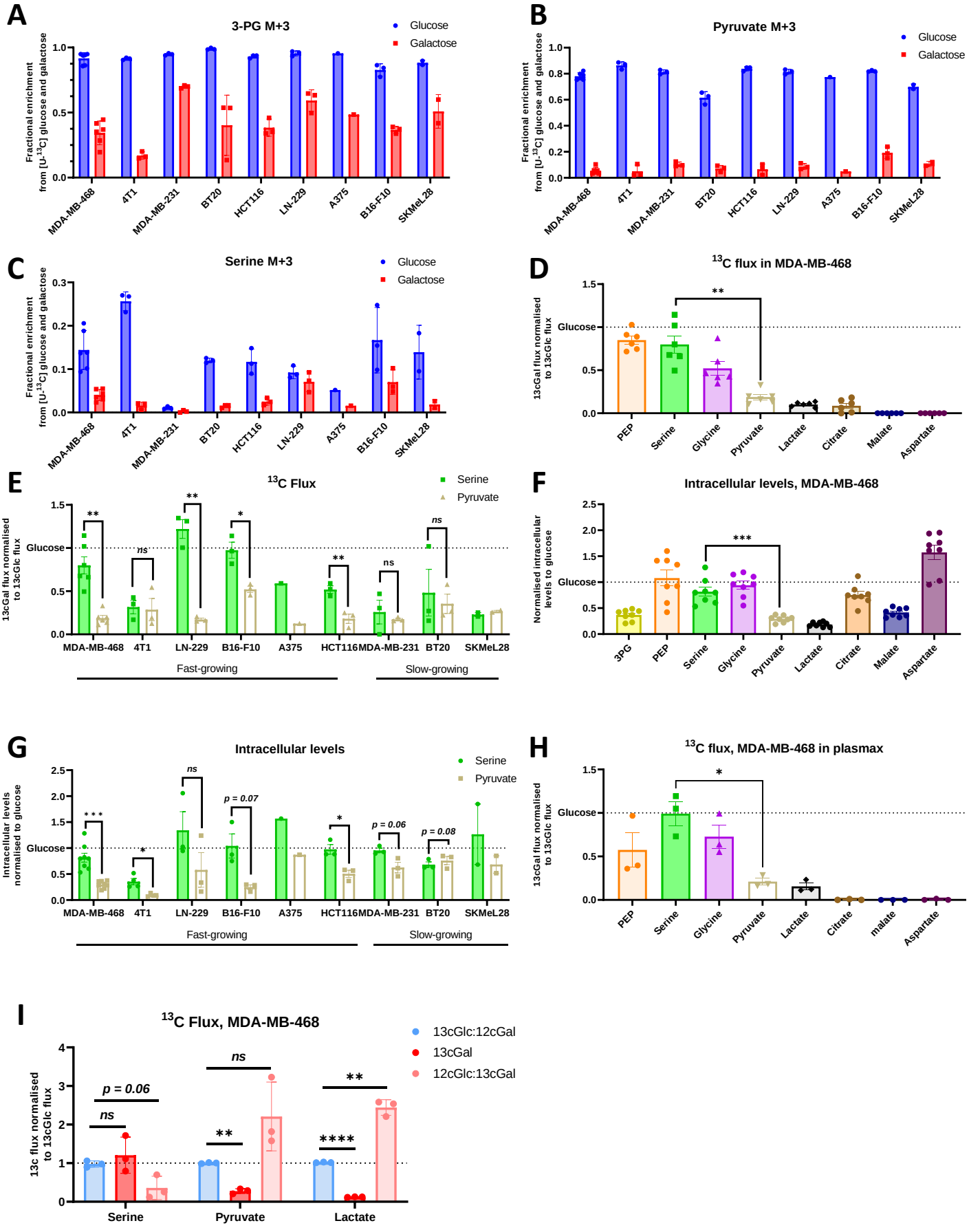
A
3-PG M+3
Glucose
Galactose
Fractional enrichment from [U-13C] glucose and galactose
MDA-MB-468
4T1
MDA-MB-231
BT20
HCT116
LN-229
A375
B16-F10
SKMeL28
B
Pyruvate M+3
C
Serine M+3
D
13C flux in MDA-MB-468
13cGal flux normalised to 13cGlc flux
Glucose
PEP
Serine
Glycine
Pyruvate
Lactate
Citrate
Malate
Aspartate
E
13C Flux
Pyruvate
Fast-growing
Slow-growing
F
Intracellular levels, MDA-MB-468
Normalised intracellular levels to glucose
3PG
G
Intracellular levels
Intracellular levels normalised to glucose
p = 0.07
p = 0.06
p = 0.08
H
13C flux, MDA-MB-468 in plasmax
I
13C Flux, MDA-MB-468
13cGlc:12cGal
13cGal
12cGlc:13cGal
13c flux normalised to 13cGlc flux
p = 0.06
ns
Serine
Pyruvate
Lactate

Figure 4. Cancer cells sustain carbon flux towards serine synthesis pathway (SSP) under glycolytic limitation. A-C Fractional enrichment from 17.5 mM [U-^{13}C] glucose and galactose into M+3 3PG (**A**), M+3 pyruvate (**B**) and M+3 serine (**C**) after 24h incubation measured with LC-MS. **D-E** The normalised relative ^{13}C flux under galactose towards multiple metabolites represented as a fold change of the same ratio under glucose in MDA-MB-468 (**D**) and a panel of 9 cancer cell lines (**E**). Fast-growing cells are those with doubling time <24h. **F-G** Intracellular levels of multiple metabolites under galactose represented as a fold change of the levels under glucose in MDA-MB-468 (**F**) and a panel of 9 cancer cell lines (**G**). **H** The normalised relative ^{13}C flux under galactose towards multiple metabolites represented as a fold change of the same ratio under glucose in MDA-MB-468 when cultured in physiological medium Plasmax. **I** The normalised relative ^{13}C flux under galactose and glucose:galactose mixes towards multiple metabolites represented as a fold change of the same ratio under glucose in MDA-MB-468. (**A-I**) Each dot represent an independent experiment (from 3 different replicate wells). (**A-I**) Mean±SEM, * $p<0.05$, ** $p<0.01$, *** $p<0.001$, **** $p<0.0001$, ns $p>0.1$. *P* value is calculated by Student's t-test, two-tailed, unpaired with Welch's correction.

Figure 5

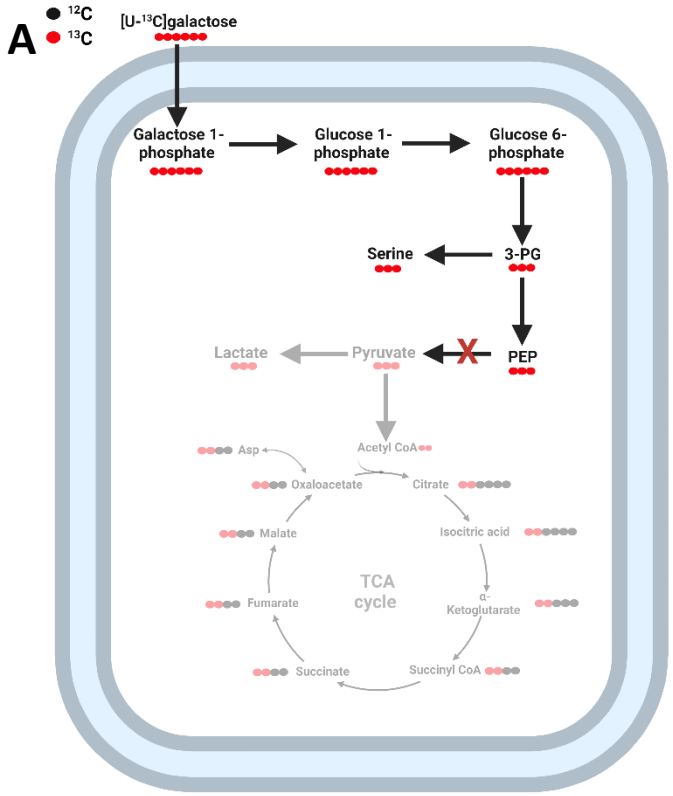
A
12C
13C
[U-13C]galactose
Galactose 1-phosphate
Glucose 1-phosphate
Glucose 6-phosphate
Serine
3-PG
PEP
Lactate
Pyruvate
Acetyl CoA
Asp
Oxaloacetate
Citrate
Malate
Isocitric acid
TCA cycle
Fumarate
α-Ketoglutarate
Succinate
Succinyl CoA

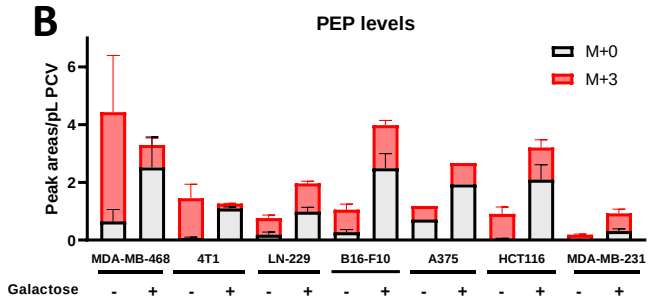
B
PEP levels
M+0
M+3
Peak areas/pL PCV
MDA-MB-468
4T1
LN-229
B16-F10
A375
HCT116
MDA-MB-231
Galactose

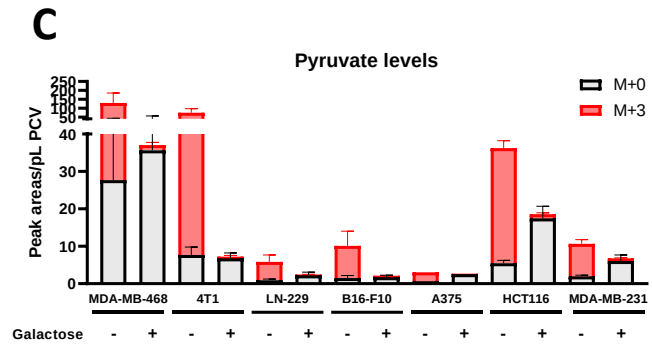
C
Pyruvate levels
M+0
M+3
Peak areas/pL PCV
MDA-MB-468
4T1
LN-229
B16-F10
A375
HCT116
MDA-MB-231
Galactose

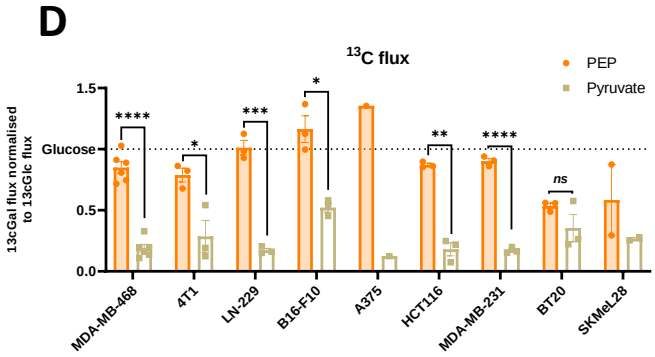
D
13C flux
PEP
Pyruvate
13cGal flux normalised to 13cGlc flux
Glucose
MDA-MB-468
4T1
LN-229
B16-F10
A375
HCT116
MDA-MB-231
BT20
SKMeL28

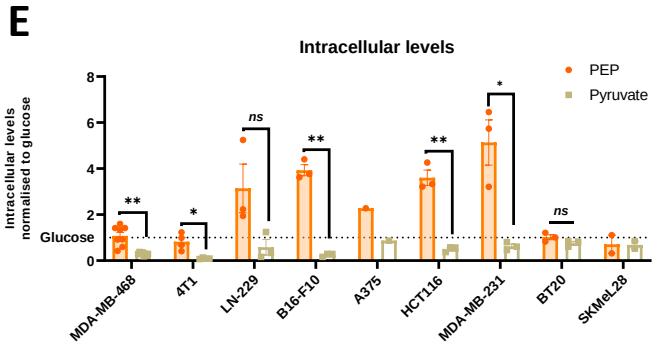
E
Intracellular levels
PEP
Pyruvate
Intracellular levels normalised to glucose
Glucose
MDA-MB-468
4T1
LN-229
B16-F10
A375
HCT116
MDA-MB-231
BT20
SKMeL28

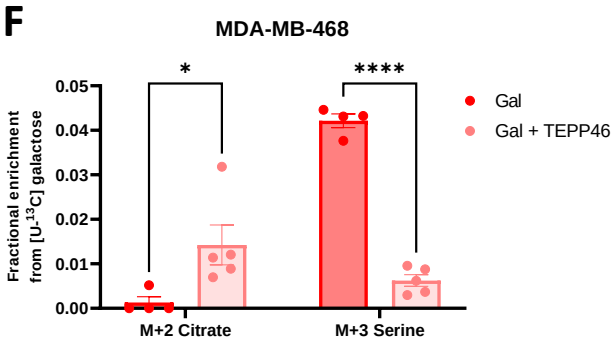
F
MDA-MB-468
Gal
Gal + TEPP46
Fractional enrichment from [U-13C] galactose
M+2 Citrate
M+3 Serine

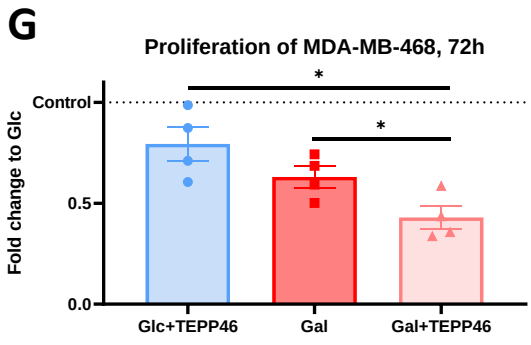
G
Proliferation of MDA-MB-468, 72h
Control
Fold change to Glc
Glc+TEPP46
Gal
Gal+TEPP46

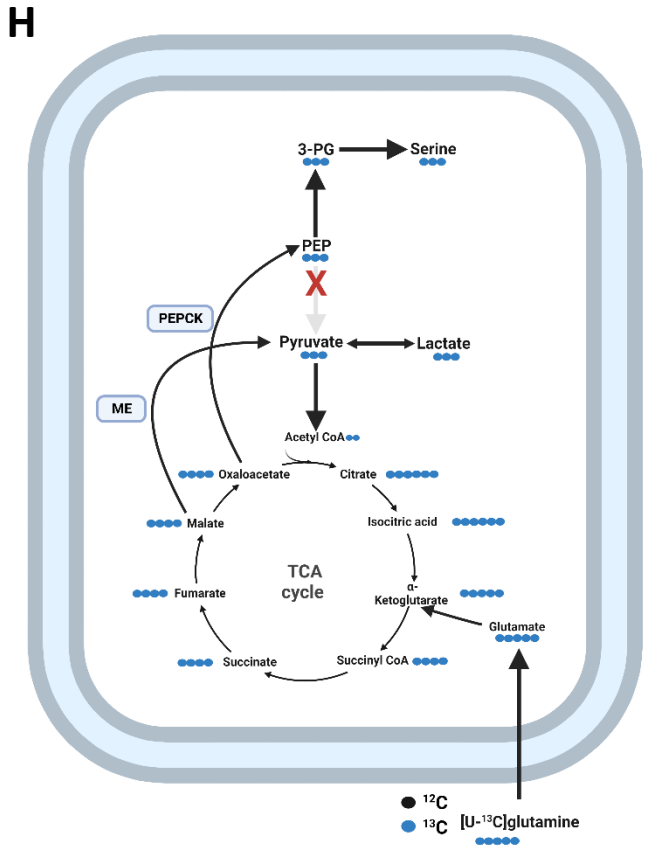
H
3-PG
Serine
PEP
PEPCK
Pyruvate
Lactate
ME
Acetyl CoA
Oxaloacetate
Citrate
Malate
Isocitric acid
TCA cycle
Fumarate
α-Ketoglutarate
Glutamate
Succinate
Succinyl CoA
12C
13C
[U-13C]glutamine

783 **Figure 5. Glycolytic limitation inhibits glycolytic flux at pyruvate kinase isozyme M2 (PKM2). A** Schematic
784 representation of glycolysis and TCA cycle upon isotopologue labelling with [U-^{13}C] glucose and galactose with the
785 proposed block at PKM2. **B-C** Peak areas of M+0 and M+3 isotopologues of PEP (**B**) and pyruvate (**C**) after 24h incubation
786 with [U-^{13}C] glucose and galactose and normalisation to packed cell volume (PCV). **D** The normalised relative ^{13}C flux
787 under galactose towards PEP and pyruvate represented as a fold change of the same ratio under glucose in a panel of
788 9 cancer cell lines. **E** Intracellular levels of PEP and pyruvate under galactose represented as a fold change of the levels
789 under glucose in a panel of 9 cancer cell lines. **F** Fractional enrichment from [U-^{13}C] galactose into M+2 citrate and M+3
790 serine after 24h incubation (Gal+TEPP-46) as measured with LC-MS. **G** 2D proliferation of MDA-MB-468 treated with
791 100 µM of TEPP-46 with either glucose or galactose and measured as cell counts at 72h relative to proliferation under
792 glucose. (**B**-**G**) Each dot represents an independent experiment (from at least 3 different replicate wells). (**B**-**G**)
793 Mean±SEM, * $p<0.05$, ** $p<0.01$, *** $p<0.001$, **** $p<0.0001$, ns $p>0.1$. *P* value is calculated by Student's t-test, two-
794 tailed, unpaired with Welch's correction. **H** Schematic representation of the rewiring of glutamine metabolism that take
795 place under glycolytic limitation and the differentiation between ME and PEPCK2 fluxes.
796

Figure 6

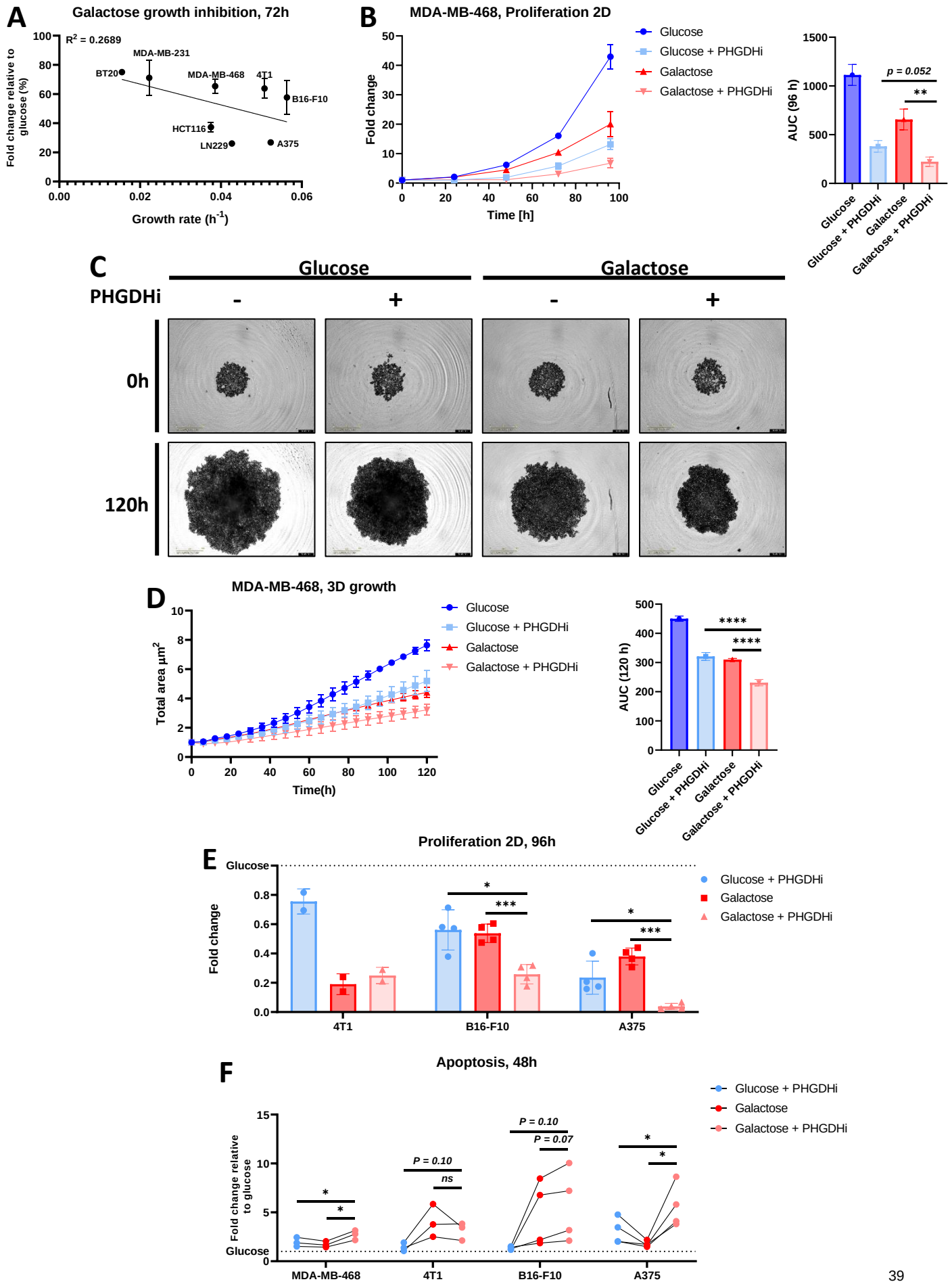
A
Galactose growth inhibition, 72h
R² = 0.2689
MDA-MB-231
BT20
MDA-MB-468
4T1
B16-F10
HCT116
LN229
A375
Fold change relative to glucose (%)
Growth rate (h⁻¹)
B
MDA-MB-468, Proliferation 2D
Fold change
Time [h]
Glucose
Glucose + PHGDHi
Galactose
Galactose + PHGDHi
AUC (96 h)
p = 0.052
**
C
Glucose
Galactose
PHGDHi
-
+
0h
120h
D
MDA-MB-468, 3D growth
Total area µm²
Time(h)
AUC (120 h)
****
E
Proliferation 2D, 96h
Fold change
4T1
B16-F10
A375
F
Apoptosis, 48h
Fold change relative to glucose
MDA-MB-468
P = 0.10
ns
P = 0.07

Figure 6. SSP is needed for proliferation and viability under glycolytic limitation. A The correlation between the growth rate of different cancer cell lines and the extent to which galactose inhibits their proliferation (represented as a percentage of growth under glucose). MDA-MB-468 n=5, 4T1 n=2, HCT116 n=2, MDA-MB-231 n=2, B16-F10 n=3, A375 n=3, BT20 n=1 and LN-229 n=1. R^2 measured for the line of best-fit using simple linear regression. **B** 2D proliferation of MDA-MB-468 when treated with 15 µM of the PHGDH inhibitor BI-4916 (PHGDHi) with either glucose or galactose, with the corresponding area under the curve (AUC). 24h and 96h timepoints include 4 independent replicates while 48h and 72h include 5 independent replicates (from at least 3 different replicate wells for each independent experiment). **C** Bright field images are representative of 3 independent experiments of MDA-MB-468 aggregates growing in anchorage-independent conditions. Scale bar represent 800 µm. **D** 3D growth of MDA-MB-468 aggregates using anchorage-independent conditions when treated with 15 µM of PHGDHi with either glucose or galactose, with the corresponding AUC. 3 independent experiments are represented each with at least 6 different replicate wells. **E** 2D proliferation of multiple cancer cell lines when treated with 15 µM of PHGDHi with either glucose or galactose as measured with cell counts at 96h relative to proliferation under glucose. Each dot represent an independent experiment from at least 3 different replicate wells. (**B**, **D, E**) Mean±SEM, * $p<0.05$, ** $p<0.01$, *** $p<0.001$, **** $p<0.0001$, n.s. $p>0.1$. *P* value is calculated by Student's t-test, two-tailed, unpaired with Welch's correction. **F** Viability of different cancer cell lines when treated with 15 µM of PHGDHi with either glucose or galactose for 48h as measured as annexin V^+ cells after excluding necrotic cells (PI). MDA-MB-468 and 4T1 n=3, B16-F10 and A375 n=4. Data shown is the mean, * $p<0.05$, ns $p>0.1$. *P* value is calculated by Student's t-test, two-tailed, paired.

Figure 7

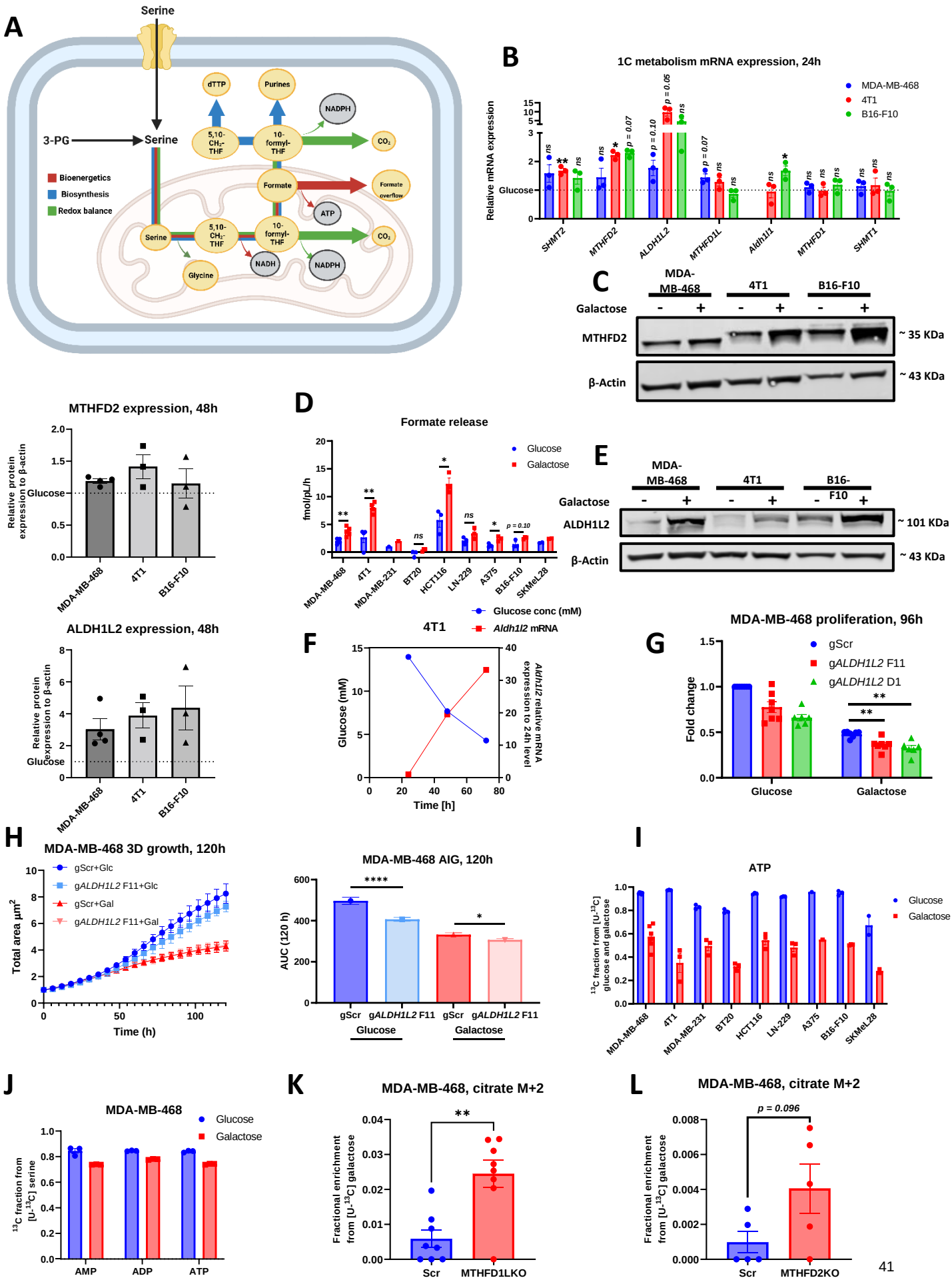
A
Serine
3-PG
Serine
dTTP
Purines
NADPH
5,10-CH2-THF
10-formyl-THF
CO2
Bioenergetics
Biosynthesis
Redox balance
Formate
Formate overflow
ATP
Serine
5,10-CH2-THF
10-formyl-THF
CO2
NADH
NADPH
Glycine
B
1C metabolism mRNA expression, 24h
MDA-MB-468
4T1
B16-F10
Relative mRNA expression
Glucose
SHMT2
MTHFD2
ALDH1L2
MTHFD1L
Aldh1l1
MTHFD1
SHMT1
C
MDA-MB-468
4T1
B16-F10
Galactose
MTHFD2
β-Actin
~ 35 KDa
~ 43 KDa
MTHFD2 expression, 48h
Relative protein expression to β-actin
Glucose
MDA-MB-468
4T1
B16-F10
D
Formate release
Glucose
Galactose
fmol/pL/h
MDA-MB-468
4T1
MDA-MB-231
BT20
HCT116
LN-229
A375
B16-F10
SKMeL28
E
MDA-MB-468
4T1
B16-F10
Galactose
ALDH1L2
β-Actin
~ 101 KDa
~ 43 KDa
ALDH1L2 expression, 48h
Relative protein expression to β-actin
Glucose
MDA-MB-468
4T1
B16-F10
F
4T1
Glucose conc (mM)
Aldh1l2 mRNA
Glucose (mM)
Aldh1l2 relative mRNA expression to 24h level
Time [h]
G
MDA-MB-468 proliferation, 96h
gScr
gALDH1L2 F11
gALDH1L2 D1
Fold change
Glucose
Galactose
H
MDA-MB-468 3D growth, 120h
gScr+Glc
gALDH1L2 F11+Glc
gScr+Gal
gALDH1L2 F11+Gal
Total area µm²
Time (h)
MDA-MB-468 AIG, 120h
AUC (120 h)
gScr
gALDH1L2 F11
gScr
gALDH1L2 F11
Glucose
Galactose
I
ATP
Glucose
Galactose
13C fraction from [U-13C] glucose and galactose
MDA-MB-468
4T1
MDA-MB-231
BT20
HCT116
LN-229
A375
B16-F10
SKMeL28
J
MDA-MB-468
Glucose
Galactose
13C fraction from [U-13C] serine
AMP
ADP
ATP
K
MDA-MB-468, citrate M+2
Fractional enrichment from [U-13C] galactose
Scr
MTHFD1LKO
L
MDA-MB-468, citrate M+2
p = 0.096
Fractional enrichment from [U-13C] galactose
Scr
MTHFD2KO

Figure 7. SSP flux is crucial to sustain mitochondrial formate production to support all three metabolic pillars. A Schematic representation of the one-carbon cycle with the different pillars and how it can contribute to biosynthesis, bioenergetic and redox balance. **B** mRNA expression of *SHMT2*, *MTHFD2*, *AALDH1L2*, *MTHFD1L*, *Aldh1l1, MTHFD1* and *SHMT1* genes relative to *GAPDH* and *ACTINβ* or *Gapdh and Sdha* after 24h incubation with either glucose or galactose measured with RT-qPCR. Data presented as fold change to the mRNA expression in cells cultured with glucose. **C** Protein expression of MTHFD2 after 48h incubation with either glucose or galactose, with the quantification of these signals relative to β-actin as a loading control and presented as a fold change of expression under galactose to that of glucose. **D** Absolute quantification of formate release from the indicated cancer cell lines after 24h incubation with either glucose or galactose. **E** Protein expression of ALDH1L2 after 48h incubation with either glucose or galactose, with the quantification of these signals relative to β-actin as a loading control and presented as a fold change of expression under galactose to that of glucose. **F** Concentration of glucose as measured in media in which 4T1 cells were cultured for 72h, compared to A*ldh1l2* mRNA expression relative to *Gapdh* and presented as fold change for expression at 24h. Data presented in **F** is from one independent experiment, mRNA was extracted from single wells while medium measurement are mean±SEM of 3 different replicate wells. **G** 2D proliferation of MDA-MB-468 Scramble and ALDH1L2KO cells cultured in either glucose or galactose as measured with cell counts at 96h relative to proliferation of scramble cells under glucose. **H** 3D growth of MDA-MB-468 control and ALDH1L2KO aggregates using anchorage-independent conditions in either glucose or galactose, with the corresponding AUC. 3 independent experiments are represented each with at least 6 different replicate wells. **I** ^{13}C fraction in ATP from [U-^{13}C] glucose and galactose after 24h incubation in multiple cell lines. **J** ^{13}C fraction in AMP/ADP/ATP from [U-^{13}C] serine after 24h incubation in MDA-MB-468. **K-L** Fractional enrichment from [U-^{13}C] galactose into M+2 citrate after 24h incubation in MDA-MB-468 Scramble compared to MTHFD1LKO (**K**) and MTHFD2KO (**L**) as measured with LC-MS. (**B-L**) Each dot represent an independent experiment averaged from 3 different replicate wells unless stated otherwise. (**B**-**L**) Mean±SEM, * $p<0.05$, ** $p<0.01$, *** $p<0.001$, **** $p<0.0001$, ns $p>0.1$. *P* value is calculated by Student's t-test, two-tailed, unpaired with Welch's correction unless stated otherwise.

Figure 8

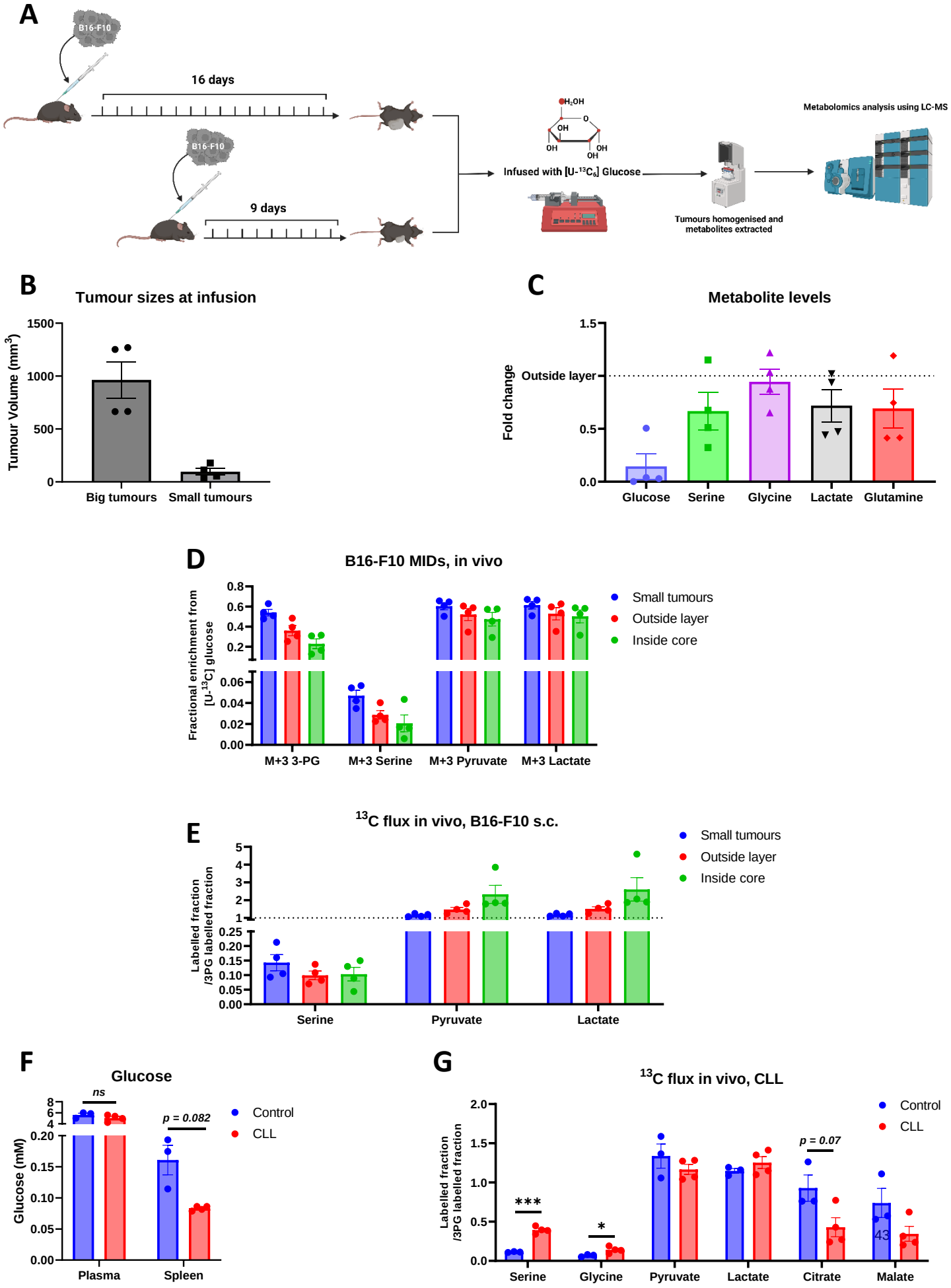
A
B16-F10
16 days
B16-F10
9 days
Infused with [U-13C6] Glucose
Tumours homogenised and metabolites extracted
Metabolomics analysis using LC-MS
B
Tumour sizes at infusion
Tumour Volume (mm3)
1500
1000
500
0
Big tumours
Small tumours
C
Metabolite levels
Fold change
1.5
Outside layer
0.5
0.0
Glucose
Serine
Glycine
Lactate
Glutamine
D
B16-F10 MIDs, in vivo
Fractional enrichment from [U-13C] glucose
0.8
0.6
0.4
0.2
0.06
0.04
0.02
0.00
M+3 3-PG
M+3 Serine
M+3 Pyruvate
M+3 Lactate
Small tumours
Outside layer
Inside core
E
13C flux in vivo, B16-F10 s.c.
Labelled fraction /3PG labelled fraction
5
4
3
2
1
0.25
0.20
0.15
0.10
0.05
0.00
Serine
Pyruvate
Lactate
Small tumours
Outside layer
Inside core
F
Glucose
ns
p = 0.082
Glucose (mM)
8
6
4
0.20
0.15
0.10
0.05
0.00
Plasma
Spleen
Control
CLL
G
13C flux in vivo, CLL
Labelled fraction /3PG labelled fraction
2.0
1.5
1.0
0.5
0.0
***
*
p = 0.07
Serine
Glycine
Pyruvate
Lactate
Citrate
Malate
Control
CLL

843 **Figure 8. *In vivo* relevance of using Gal to model glycolytic limitation**. **A** Schematic representation of the *in vivo*
844 setup for B16-F10 subcutaneous tumours. **B** Tumour volume of B16-F10 tumours grown subcutaneously on the flanks
845 of C57BL/6 mice (n=4/group). **C** Metabolite levels measured from the inside core of B16-F10 tumours and presented as
846 fold change of the level of those metabolites in the outside layer of the same tumours. **D** Fractional enrichment in
847 tumour piece of the presented metabolites after 2h infusion with [U-^{13}C] glucose via the tail vain. **E** The ^{13}C flux from 3-
848 PG towards multiple metabolites measured in B16-F10 tumours. **F** Glucose concentration as measured in the plasma
849 and in grinded spleen tissue from control and CLL mice after 2h continuous infusion with [U-^{13}C] glucose. The
850 concentration was determined using standard addition method. **G** The ^{13}C flux from 3-PG towards multiple metabolites
851 measured in CLL cells collected from the spleen of CLL mice. (**B-G**) Each dot represent a biological replicate. (**A-F**)
852 Mean±SEM, * $p<0.05$, ** $p<0.01$, *** $p<0.001$, **** $p<0.0001$, ns $p>0.1$. *P* value is calculated by Student's t-test, two-
853 tailed, unpaired with Welch's correction unless stated otherwise.
854

Figure S1

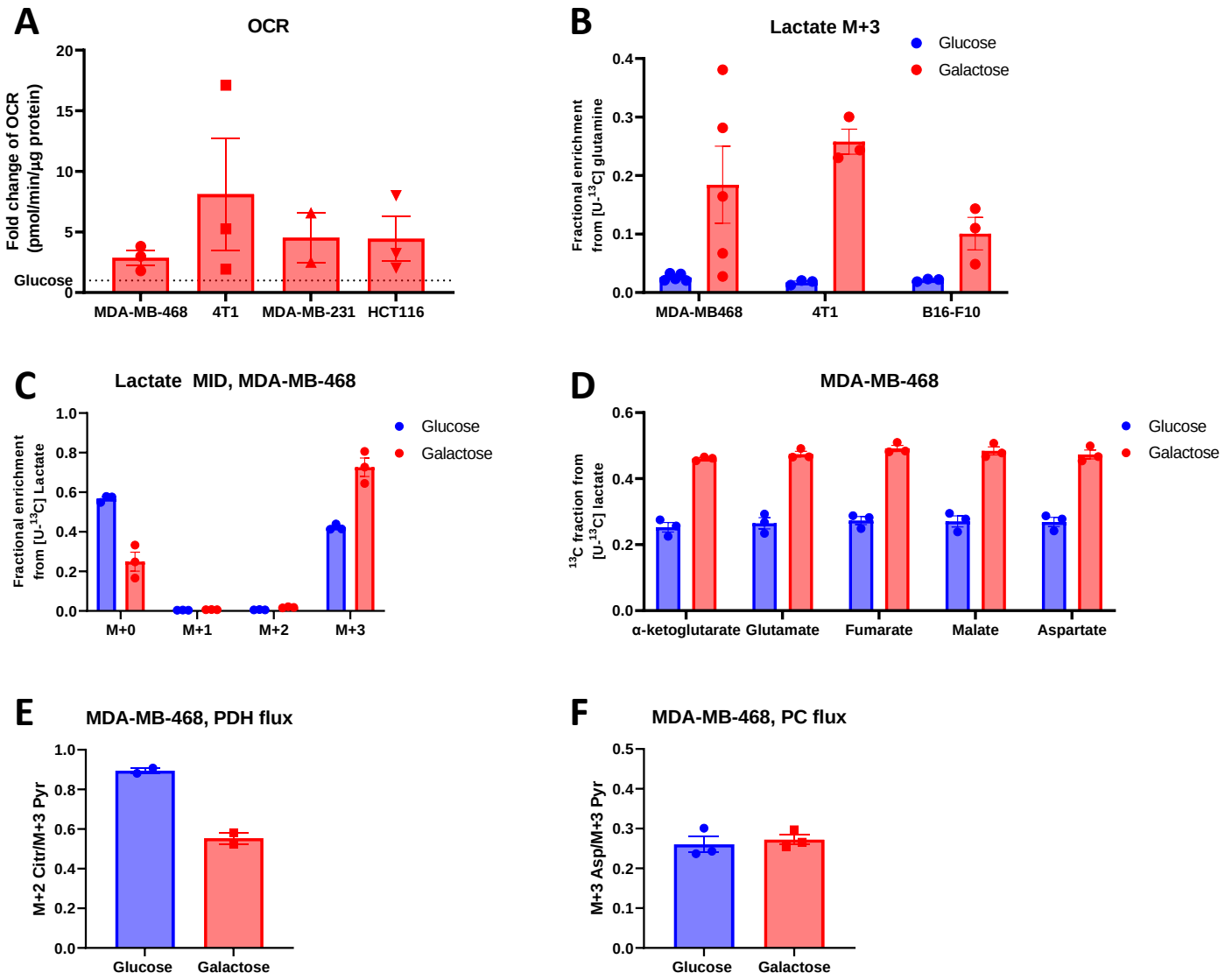
A
OCR
Fold change of OCR (pmol/min/µg protein)
Glucose
MDA-MB-468
4T1
MDA-MB-231
HCT116
B
Lactate M+3
Glucose
Galactose
Fractional enrichment from [U-13C] glutamine
MDA-MB468
4T1
B16-F10
C
Lactate MID, MDA-MB-468
Fractional enrichment from [U-13C] Lactate
Glucose
Galactose
M+0
M+1
M+2
M+3
D
MDA-MB-468
13C fraction from [U-13C] lactate
Glucose
Galactose
α-ketoglutarate
Glutamate
Fumarate
Malate
Aspartate
E
MDA-MB-468, PDH flux
M+2 Citr/M+3 Pyr
Glucose
Galactose
F
MDA-MB-468, PC flux
M+3 Asp/M+3 Pyr
Glucose
Galactose

856 **Supplementary Figure 1. A** Basal oxygen consumption rate (OCR) measured by seahorse in 4 different cancer cell lines
857 after 24h incubation with galactose and presented as fold change to the same measurements with glucose. **B** Fractional
858 enrichment in M+3 lactate from [U-^{13}C] glutamine after 24h incubation with either glucose or galactose medium in
859 MDA-MB-468, 4T1 and B16-F10. **C** Fractional enrichment in lactate from [U-^{13}C] sodium lactate after 24h incubation
860 with either glucose or galactose medium in MDA-MB-468. **D** ^{13}C fraction in TCA cycle metabolites from [U-^{13}C] sodium
861 lactate after 24h incubation with either glucose or galactose medium in MDA-MB-468. **E** Pyruvate dehydrogenase (PDH)
862 enzyme flux ratio calculated as M+2 citrate/M+3 pyruvate isotopologues from [U-^{13}C] sodium lactate after 24h
863 incubation with either glucose or galactose medium in MDA-MB-468. **F** Pyruvate carboxylase (PC) enzyme flux ratio
864 calculated as M+3 aspartate/M+3 pyruvate isotopologues from [U-^{13}C] sodium lactate after 24h incubation with either
865 glucose or galactose medium in MDA-MB-468. (**A-F**) Each dot represents an independent experiment averaged from 3
866 different replicate wells. (**A-F**) Mean±SEM, * $p<0.05$, ** $p<0.01$, *** $p<0.001$, **** $p<0.0001$, ns $p>0.1$. *P* value is
867 calculated by Student's t-test, two-tailed, unpaired with Welch's correction.
868

Figure S2

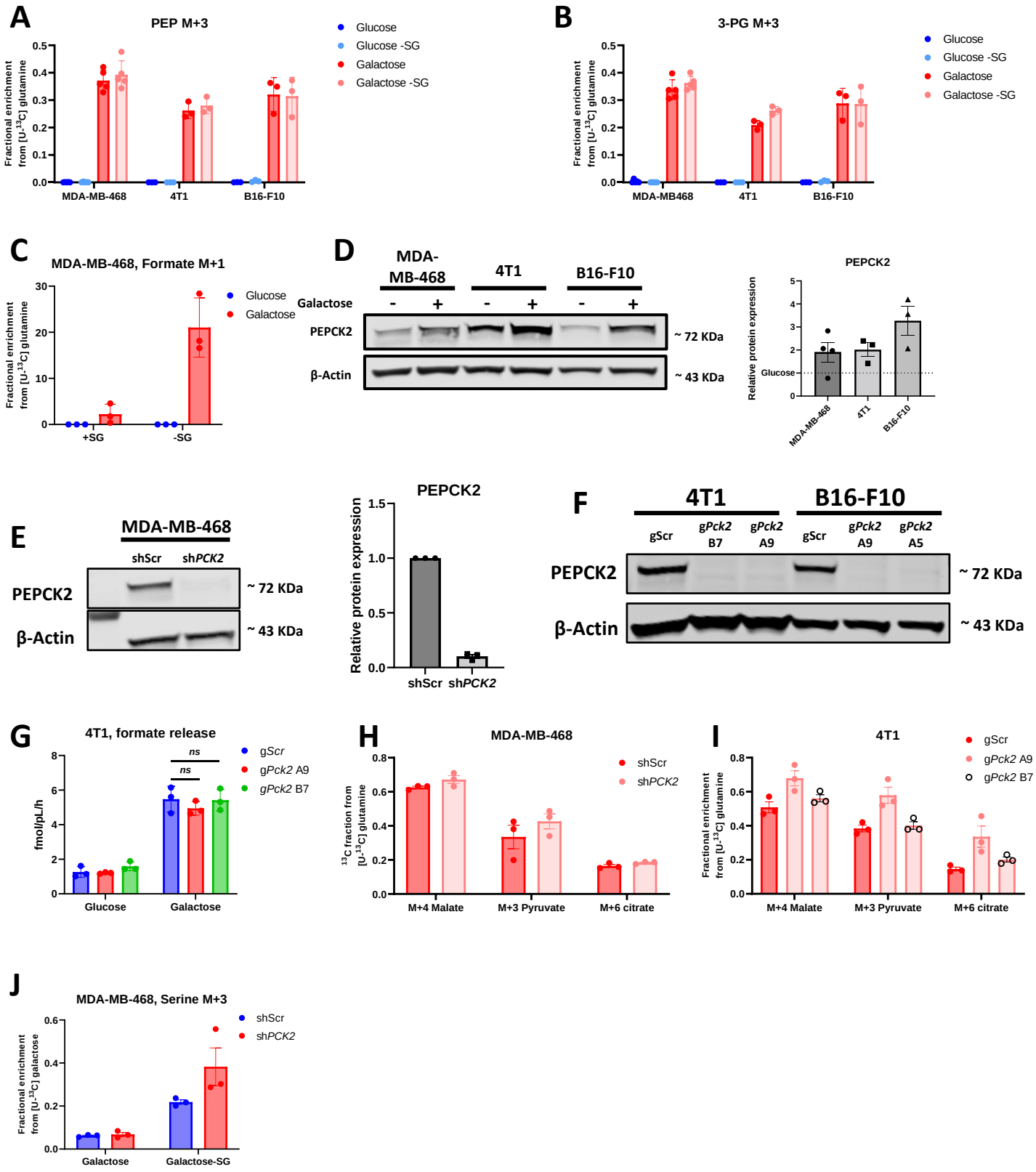
A
PEP M+3
Fractional enrichment from [U-13C] glutamine
MDA-MB-468
4T1
B16-F10
Glucose
Glucose -SG
Galactose
Galactose -SG
B
3-PG M+3
Fractional enrichment from [U-13C] glutamine
MDA-MB468
4T1
B16-F10
Glucose
Glucose -SG
Galactose
Galactose -SG
C
MDA-MB-468, Formate M+1
Fractional enrichment from [U-13C] glutamine
+SG
-SG
Glucose
Galactose
D
MDA-MB-468
4T1
B16-F10
Galactose
PEPCK2
β-Actin
~ 72 KDa
~ 43 KDa
PEPCK2
Relative protein expression
Glucose
MDA-MB-468
4T1
B16-F10
E
MDA-MB-468
shScr
shPCK2
PEPCK2
β-Actin
~ 72 KDa
~ 43 KDa
PEPCK2
Relative protein expression
shScr
shPCK2
F
4T1
B16-F10
gScr
gPck2 B7
gPck2 A9
gScr
gPck2 A9
gPck2 A5
PEPCK2
β-Actin
~ 72 KDa
~ 43 KDa
G
4T1, formate release
fmol/pL/h
ns
ns
Glucose
Galactose
gScr
gPck2 A9
gPck2 B7
H
MDA-MB-468
13C fraction from [U-13C] glutamine
M+4 Malate
M+3 Pyruvate
M+6 citrate
shScr
shPCK2
I
4T1
Fractional enrichment from [U-13C] glutamine
M+4 Malate
M+3 Pyruvate
M+6 citrate
gScr
gPck2 A9
gPck2 B7
J
MDA-MB-468, Serine M+3
Fractional enrichment from [U-13C] galactose
Galactose
Galactose-SG
shScr
shPCK2

870 **Supplementary Figure 2. A-B** Fractional enrichment in M+3 PEP **(A)** and M+3 3-PG **(B)** from [U-^{13}C] glutamine after
871 24h incubation with either glucose ± serine and glycine (SG) or galactose ± SG medium in MDA-MB-468, 4T1 and B16-
872 F10. **C** Fractional enrichment in M+1 formate from [U-^{13}C] glutamine after 24h incubation with either glucose ±
873 serine and glycine (SG) or galactose ± SG medium in MDA-MB-468. **D** Protein expression of PEPCK2 after 48h incubation
874 with either glucose or galactose, with the corresponding quantification of signal intensities relative to β-actin as a
875 loading control and presented as a fold change of expression under galactose to that of glucose. **E-F** Protein expression
876 of PEPCK2 comparing scramble to PEPCK2 KD/KOs, with the corresponding quantification of these signals relative to β-
877 actin as a loading control. **G** Absolute quantification of formate release from 4T1 after 24h incubation with either
878 glucose or galactose. **H-I** Fractional enrichment in M+4 malate, M+3 pyruvate and M+6 citrate from [U-^{13}C] glutamine
879 after 24h incubation with galactose + SG medium and comparison between control and MDA-MB-468 PEPCK2 KD **(H)**
880 and 4T1 PEPCK2 KOs **(I)**. **J** Fractional enrichment in M+3 serine from [U-^{13}C] galactose after 24h incubation with galactose
881 ± SG medium in MDA-MB-468 shScramble and sh*PCK2*. (**A-J**) Each dot represents an independent experiment averaged
882 from 3 different replicate wells replicate unless stated otherwise. (**A-J**) Mean±SEM, * $p<0.05$, ** $p<0.01$, *** $p<0.001$,
883 **** $p<0.0001$, ns $p>0.1$. *P* value is calculated by Student's t-test, two-tailed, unpaired with Welch's correction unless
884 stated otherwise.

Figure S3

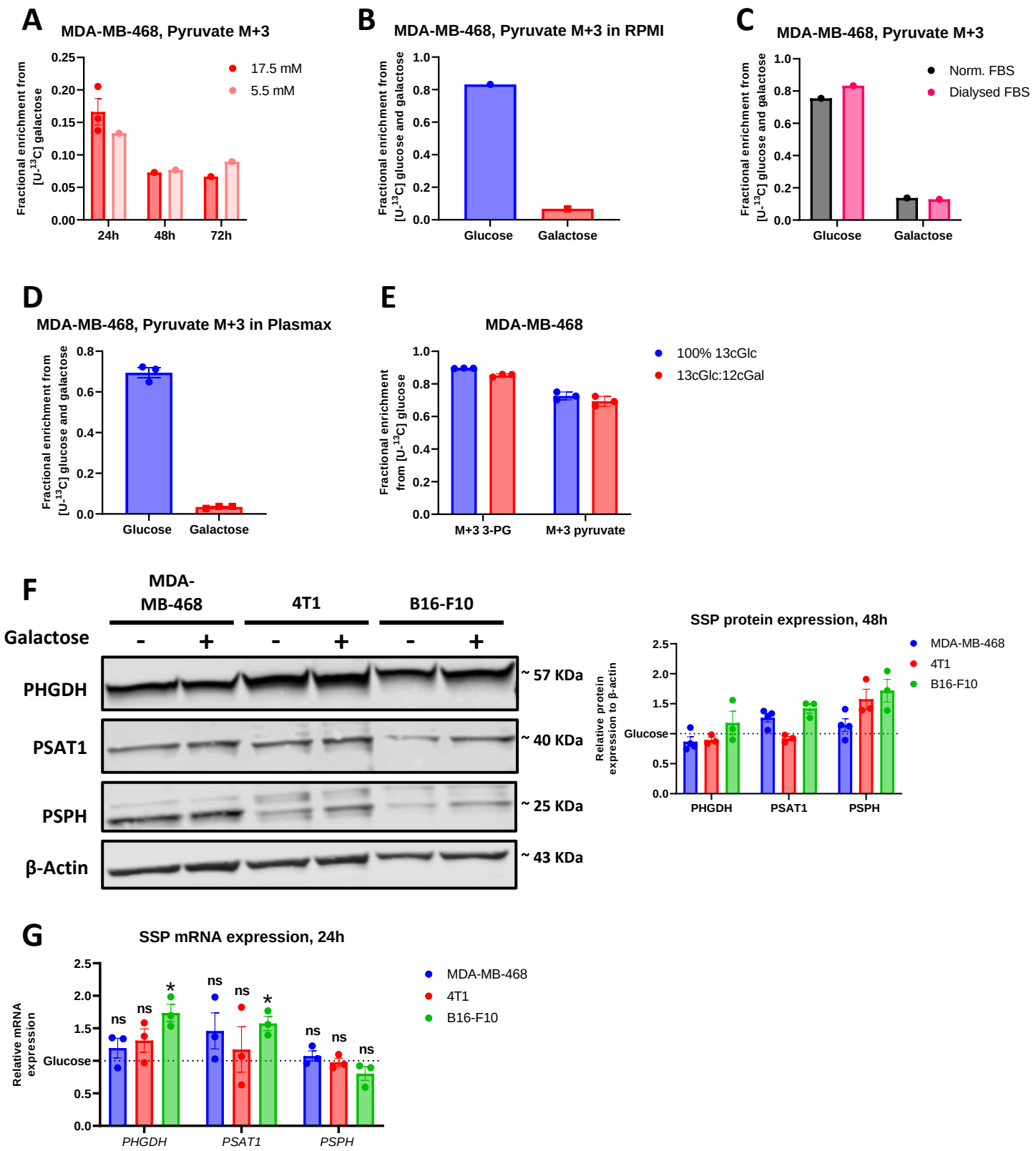
A
MDA-MB-468, Pyruvate M+3
Fractional enrichment from [U-13C] galactose
17.5 mM
5.5 mM
24h
48h
72h
B
MDA-MB-468, Pyruvate M+3 in RPMI
Fractional enrichment from [U-13C] glucose and galactose
Glucose
Galactose
C
MDA-MB-468, Pyruvate M+3
Fractional enrichment from [U-13C] glucose and galactose
Norm. FBS
Dialysed FBS
Glucose
Galactose
D
MDA-MB-468, Pyruvate M+3 in Plasmax
Fractional enrichment from [U-13C] glucose and galactose
Glucose
Galactose
E
MDA-MB-468
Fractional enrichment from [U-13C] glucose
100% 13cGlc
13cGlc:12cGal
M+3 3-PG
M+3 pyruvate
F
MDA-MB-468
4T1
B16-F10
Galactose
PHGDH
PSAT1
PSPH
β-Actin
~ 57 KDa
~ 40 KDa
~ 25 KDa
~ 43 KDa
SSP protein expression, 48h
Relative protein expression to β-actin
MDA-MB-468
4T1
B16-F10
Glucose
PHGDH
PSAT1
PSPH
G
SSP mRNA expression, 24h
Relative mRNA expression
MDA-MB-468
4T1
B16-F10
Glucose
PHGDH
PSAT1
PSPH

886 **Supplementary Figure 3. A** Fractional enrichment into M+3 pyruvate using [U-^{13}C] galactose after 24, 48, and 72 hour
887 incubation and using 17.5 or 5.5 mM of the tracer in MDA-MB-468. **B** Fractional enrichment into M+3 pyruvate using
888 [U-^{13}C] glucose and galactose in RPMI1640 in MDA-MB-468 with 10% dialysed FBS. **C** Fractional enrichment into M+3
889 pyruvate using [U-^{13}C] glucose and galactose after 24 hour incubation and using 17.5 mM of the tracer in MDA-MB-468
890 with 10% FBS or 10% dialysed FBS. **D** Fractional enrichment into M+3 pyruvate using [U-^{13}C] glucose and galactose in
891 physiological medium Plasmax in MDA-MB-468. **E** Fractional enrichment from 17.5 mM [U-^{13}C] glucose into M+3 3PG
892 and M+3 pyruvate after 24h incubation measured with LC-MS. **F** Protein expression of PHGDH, PSAT and PSPH after 48h
893 incubation with either glucose or galactose, with the quantification of signal intensities relative to β-actin as a loading
894 control and shown as a fold change of expression under galactose to that of glucose. **G** mRNA expression of *PHGDH*,
895 *PSAT1*, *PSPH* relative to *GAPDH* and *ACTINβ* or *Gapdh and Sdha* after 24h incubation with either glucose or galactose
896 measured with RT-qPCR. Data presented as fold change to the mRNA expression in cells cultured with glucose. (**A**-**G**)
897 Each dot represent an independent experiment (**A-E** each independent experiment is from at least 3 different replicate
898 wells). (**A**-**G**) Mean±SEM, * $p<0.05$, ** $p<0.01$, *** $p<0.001$, **** $p<0.0001$, ns $p>0.1$. *P* value is calculated by Student's
899 t-test, two-tailed, unpaired with Welch's correction.

Figure S4

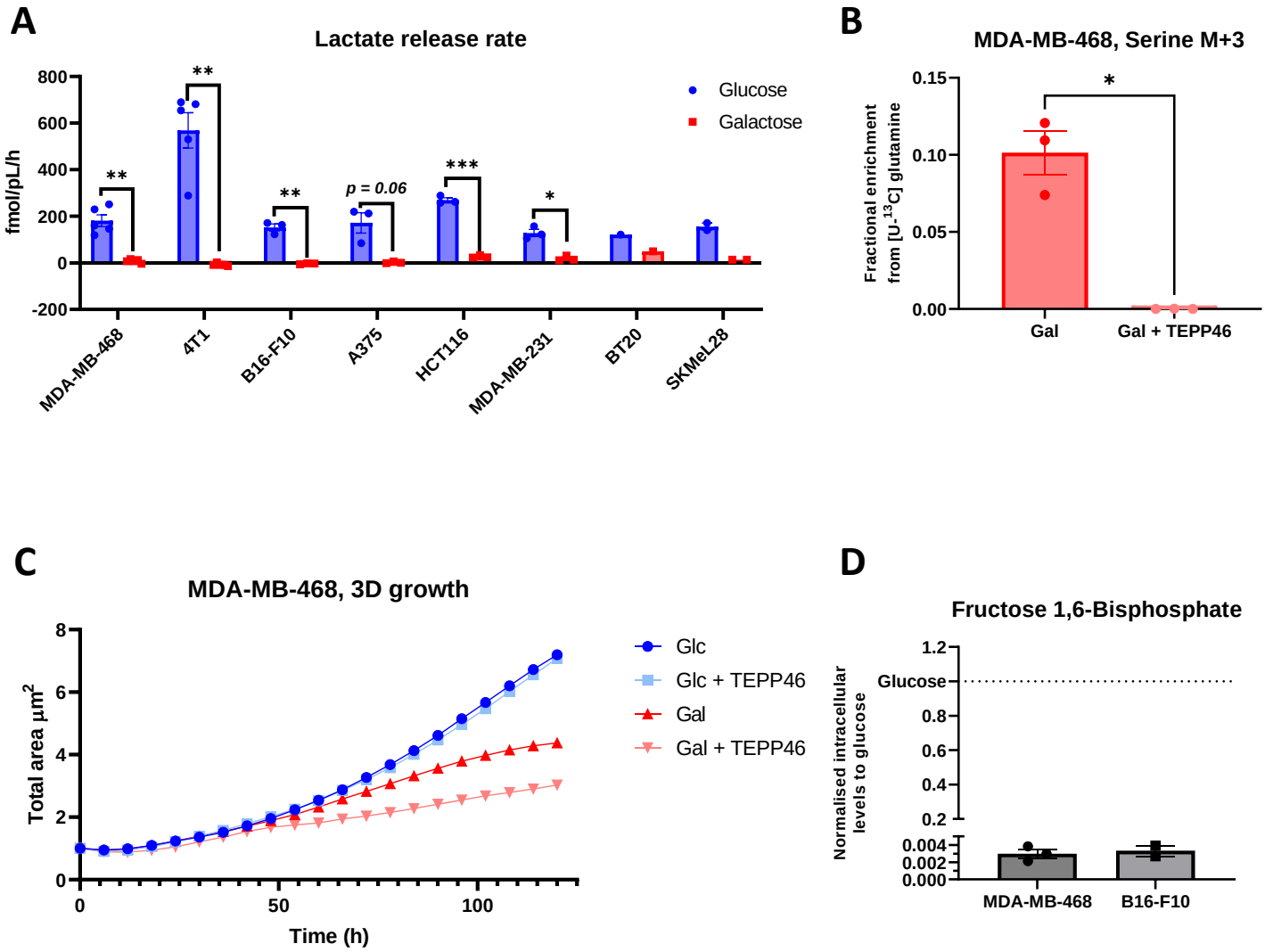
A
Lactate release rate
fmol/pL/h
800
600
400
200
0
-200
**
**
**
p = 0.06
***
*
Glucose
Galactose
MDA-MB-468
4T1
B16-F10
A375
HCT116
MDA-MB-231
BT20
SKMeL28
B
MDA-MB-468, Serine M+3
Fractional enrichment from [U-13C] glutamine
0.15
0.10
0.05
0.00
*
Gal
Gal + TEPP46
C
MDA-MB-468, 3D growth
Total area µm2
8
6
4
2
0
0
50
100
Time (h)
Glc
Glc + TEPP46
Gal
Gal + TEPP46
D
Fructose 1,6-Bisphosphate
Normalised intracellular levels to glucose
1.2
Glucose
0.8
0.6
0.4
0.2
0.004
0.002
0.000
MDA-MB-468
B16-F10

Supplementary Figure 4. A Absolute quantification of lactate released into the medium per hour of incubation with normalisation to packed cell volume per condition in either glucose or galactose in multiple cancer cell lines. **B** Fractional enrichment from [U-^{13}C] glutamine into M+3 serine after 24h incubation measured with LC-MS. **C** 3D growth of MDA-MB-468 aggregates using anchorage-independent conditions when treated with 100 µM of TEPP-46 with either glucose or galactose. 1 independent experiment is represented with at least 6 different replicate wells. **D** Intracellular levels of fructose 1,6-BP under galactose represented as a fold change of the levels under glucose in MDA-MB-468 and B16-F10. (**A**, **B** and **D**) Each dot represent an independent experiment (from 3 different replicate wells). (**A**-**C**) Mean±SEM, * $p<0.05$, ** $p<0.01$, *** $p<0.001$, **** $p<0.0001$, ns $p>0.1$. *P* value is calculated by Student's t-test, two-tailed, unpaired with Welch's correction.

Figure S5

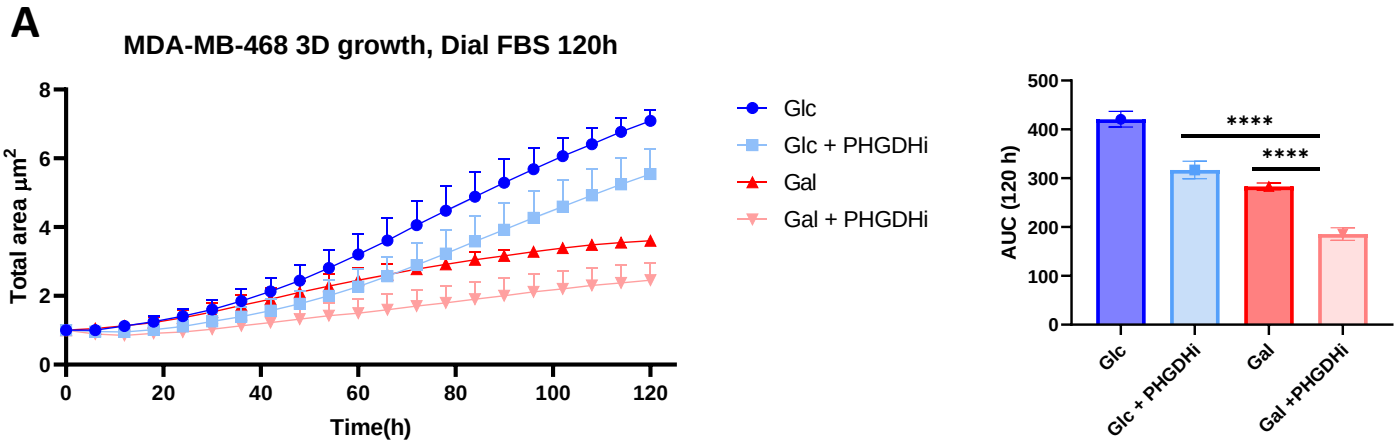
A
MDA-MB-468 3D growth, Dial FBS 120h
Total area µm²
Time(h)
0
2
4
6
8
0
20
40
60
80
100
120
Glc
Glc + PHGDHi
Gal
Gal + PHGDHi
AUC (120 h)
500
400
300
200
100
0
****
****
Glc
Glc + PHGDHi
Gal
Gal +PHGDHi

Supplementary Figure 5. A 3D growth of MDA-MB-468 aggregates using anchorage-independent conditions when treated with 15 µM of PHGDHi with either glucose or galactose with 10% dialysed FBS, with the corresponding AUC. 3 independent experiments are represented each with at least 6 replicate wells. Mean±SEM, * $p<0.05$, ** $p<0.01$, *** $p<0.001$, **** $p<0.0001$, ns $p>0.1$. *P* value is calculated by Student's t-test, two-tailed, unpaired with Welch's correction.

Figure S6

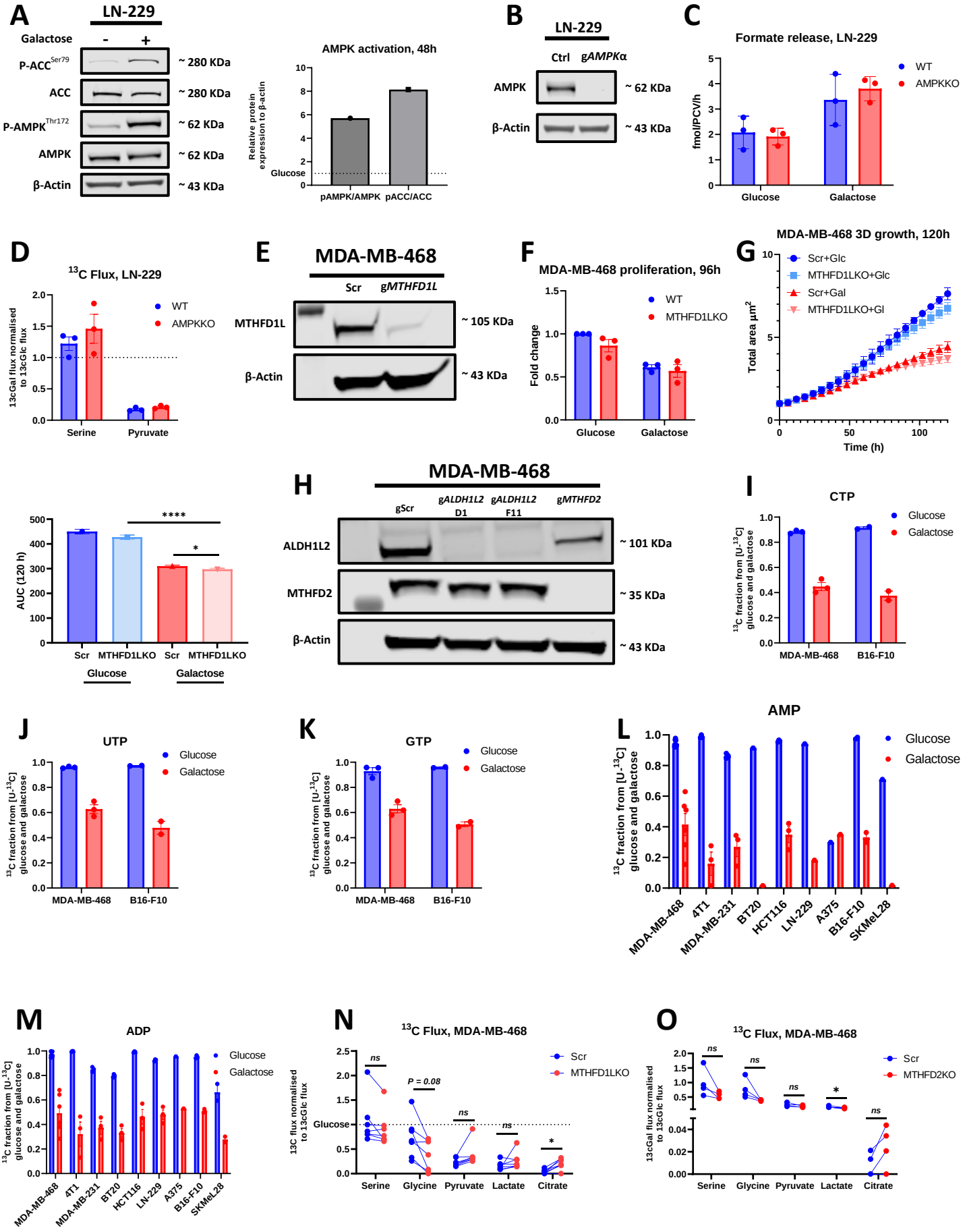
A
LN-229
Galactose - +
P-ACC Ser79
ACC
P-AMPK Thr172
AMPK
β-Actin
~ 280 KDa
~ 280 KDa
~ 62 KDa
~ 62 KDa
~ 43 KDa
AMPK activation, 48h
Relative protein expression to β-actin
Glucose
pAMPK/AMPK
pACC/ACC
B
LN-229
Ctrl gAMPKα
AMPK
β-Actin
~ 62 KDa
~ 43 KDa
C
Formate release, LN-229
fmol/PCV/h
WT
AMPKKO
Glucose
Galactose
D
13C Flux, LN-229
13cGal flux normalised to 13cGlc flux
WT
AMPKKO
Serine
Pyruvate
E
MDA-MB-468
Scr gMTHFD1L
MTHFD1L
β-Actin
~ 105 KDa
~ 43 KDa
F
MDA-MB-468 proliferation, 96h
Fold change
WT
MTHFD1LKO
Glucose
Galactose
G
MDA-MB-468 3D growth, 120h
Scr+Glc
MTHFD1LKO+Glc
Scr+Gal
MTHFD1LKO+Gl
Total area µm2
Time (h)
AUC (120 h)
****
*
Scr MTHFD1LKO Scr MTHFD1LKO
Glucose
Galactose
H
MDA-MB-468
gScr gALDH1L2 D1 gALDH1L2 F11 gMTHFD2
ALDH1L2
MTHFD2
β-Actin
~ 101 KDa
~ 35 KDa
~ 43 KDa
I
CTP
13C fraction from [U-13C] glucose and galactose
Glucose
Galactose
MDA-MB-468
B16-F10
J
UTP
Glucose
Galactose
MDA-MB-468
B16-F10
K
GTP
Glucose
Galactose
MDA-MB-468
B16-F10
L
AMP
Glucose
Galactose
MDA-MB-468
4T1
MDA-MB-231
BT20
HCT116
LN-229
A375
B16-F10
SKMeL28
M
ADP
Glucose
Galactose
MDA-MB-468
4T1
MDA-MB-231
BT20
HCT116
LN-229
A375
B16-F10
SKMeL28
N
13C Flux, MDA-MB-468
13C flux normalised to 13cGlc flux
Scr
MTHFD1LKO
ns
P = 0.08
ns
ns
*
Glucose
Serine
Glycine
Pyruvate
Lactate
Citrate
O
13C Flux, MDA-MB-468
13cGal flux normalised to 13cGlc flux
Scr
MTHFD2KO
ns
ns
ns
*
ns
Serine
Glycine
Pyruvate
Lactate
Citrate

Supplementary Figure 6. A Protein expression of p-AMPK, AMPK, p-ACC and ACC in LN-229 after 48h incubation with either glucose or galactose, with the quantification of signal intensities relative to β-actin as a loading control and shown as a fold change of expression under galactose to that of glucose. **B** Protein expression of AMPK comparing control to the corresponding KO with β-actin as a loading control. **C** Absolute quantification of formate release from LN-229 control and AMPKKO after 24h incubation with either glucose or galactose. **D** The normalised relative ^{13}C flux under galactose towards serine and pyruvate is represented as a fold change of the same ratio under glucose in LN-229 control and AMPKKO. **E** Protein expression of MTHFD1L comparing scramble to the corresponding KO with β-actin as a loading control. **F** 2D proliferation of MDA-MB-468 Scramble and MTHFD1LKO cells cultured in either glucose or galactose as measured with cell counts at 96h relative to proliferation of scramble cells under glucose. **G** 3D growth of MDA-MB-468 control and MTHFD1LKO cell aggregates using anchorage-independent conditions in either glucose or galactose, with the corresponding AUC. 3 independent experiments are represented each with at least 6 different replicate wells. **H** Protein expression of MTHFD2 and ALDH1L2 comparing scramble to the corresponding KOs with β-actin as a loading control. **I-K** Fractional enrichment in CTP **(I)**, UTP **(J)** and GTP **(K)** from [U-^{13}C] glucose and galactose after 24h incubation. Data shown is the mean±SEM of 3 (MDA-MB-468) or 2 (B16-F10) independent experiments each being the average of 3 different replicate wells. **L-M** ^{13}C fraction in AMP **(L)** and ADP **(M)** from [U-^{13}C] glucose and galactose after 24h incubation in multiple cell lines. **N**-**O** The normalised relative ^{13}C flux under galactose towards multiple metabolites represented as a fold change of the same ratio under glucose in MDA-MB-468 scramble compared to MTHFD1LKO (**N**) and MTHFD2KO (**O**). (**A, C-D, F and I-O**) each dot represent an independent experiment averaged from 3 different replicate wells unless stated otherwise. (**A-O**) Mean±SEM, * $p<0.05$, ** $p<0.01$, *** $p<0.001$, **** $p<0.0001$, ns $p>0.1$. *P* value is calculated by Student's t-test, two-tailed, unpaired with Welch's correction unless stated otherwise.

References:

1. Crabtree, H.G., *Observations on the carbohydrate metabolism of tumours.* Biochem J, 1929. **23**(3): p. 536-45.
2. Hanahan, D. and R.A. Weinberg, *Hallmarks of cancer: the next generation.* Cell, 2011. **144**(5): p. 646-74.
3. Warburg, O., *The Metabolism of Carcinoma Cells1.* The Journal of Cancer Research, 1925. **9**(1): p. 148-163.
4. Vander Heiden, M.G., L.C. Cantley, and C.B. Thompson, *Understanding the Warburg effect: the metabolic requirements of cell proliferation.* Science, 2009. **324**(5930): p. 1029-33.
5. Amendola, C.R., et al., *KRAS4A directly regulates hexokinase 1.* Nature, 2019. **576**(7787): p. 482-486.
6. Fernandez-de-Cossio-Diaz, J. and A. Vazquez, *Limits of aerobic metabolism in cancer cells.* Sci Rep, 2017. **7**(1): p. 13488.
7. Locasale, J.W., et al., *Phosphoglycerate dehydrogenase diverts glycolytic flux and contributes to oncogenesis.* Nat Genet, 2011. **43**(9): p. 869-74.
8. Osthus, R.C., et al., *Deregulation of glucose transporter 1 and glycolytic gene expression by c-Myc.* J Biol Chem, 2000. **275**(29): p. 21797-800.
9. Vazquez, A., et al., *Catabolic efficiency of aerobic glycolysis: The Warburg effect revisited.* BMC Systems Biology, 2010. **4**(1): p. 58.
10. Ying, H., et al., *Oncogenic Kras maintains pancreatic tumors through regulation of anabolic glucose metabolism.* Cell, 2012. **149**(3): p. 656-70.
11. de Alteriis, E., et al., *Revisiting the Crabtree/Warburg effect in a dynamic perspective: a fitness advantage against sugar-induced cell death.* Cell Cycle, 2018. **17**(6): p. 688-701.
12. Luengo, A., et al., *Increased demand for NAD(+) relative to ATP drives aerobic glycolysis.* Mol Cell, 2021. **81**(4): p. 691-707.e6.
13. Wang, Y., et al., *Saturation of the mitochondrial NADH shuttles drives aerobic glycolysis in proliferating cells.* Molecular Cell, 2022. **82**(17): p. 3270-3283.e9.
14. Bergers, G. and S.M. Fendt, *The metabolism of cancer cells during metastasis.* Nat Rev Cancer, 2021. **21**(3): p. 162-180.
15. Fendt, S.-M., C. Frezza, and A. Erez, *Targeting Metabolic Plasticity and Flexibility Dynamics for Cancer Therapy.* Cancer Discovery, 2020. **10**(12): p. 1797-1807.
16. Cantor, J.R., *The Rise of Physiologic Media.* Trends in Cell Biology, 2019. **29**(11): p. 854-861.
17. Díaz-Ruiz, R., et al., *Mitochondrial oxidative phosphorylation is regulated by fructose 1,6-bisphosphate. A possible role in Crabtree effect induction?* J Biol Chem, 2008. **283**(40): p. 26948-55.
18. Holden, H.M., I. Rayment, and J.B. Thoden, *Structure and function of enzymes of the Leloir pathway for galactose metabolism.* J Biol Chem, 2003. **278**(45): p. 43885-8.
19. Rempel, A., et al., *Glucose catabolism in cancer cells: amplification of the gene encoding type II hexokinase.* Cancer Res, 1996. **56**(11): p. 2468-71.
20. Wilson, J.E., *Isozymes of mammalian hexokinase: structure, subcellular localization and metabolic function.* Journal of Experimental Biology, 2003. **206**(12): p. 2049-2057.
21. Timson, D.J. and R.J. Reece, *Functional analysis of disease-causing mutations in human galactokinase.* European Journal of Biochemistry, 2003. **270**(8): p. 1767-1774.
22. Sullivan, M.R., et al., *Quantification of microenvironmental metabolites in murine cancers reveals determinants of tumor nutrient availability.* eLife, 2019. **8**: p. e44235.
23. Reinfeld, B.I., et al., *Cell-programmed nutrient partitioning in the tumour microenvironment.* Nature, 2021. **593**(7858): p. 282-288.
24. Meiser, J., et al., *Serine one-carbon catabolism with formate overflow.* Sci Adv, 2016. **2**(10): p. e1601273.
25. Benzarti, M., et al., *Metabolic Potential of Cancer Cells in Context of the Metastatic Cascade.* Cells, 2020. **9**(9).

26. Hyroššová, P., et al., *PEPCK-M recoups tumor cell anabolic potential in a PKC-ζ-dependent manner.* Cancer Metab, 2021. **9**(1): p. 1.
27. Keshet, R., et al., *Targeting purine synthesis in ASS1-expressing tumors enhances the response to immune checkpoint inhibitors.* Nature Cancer, 2020. **1**(9): p. 894-908.
28. Leithner, K., et al., *PCK2 activation mediates an adaptive response to glucose depletion in lung cancer.* Oncogene, 2015. **34**(8): p. 1044-50.
29. Vincent, E.E., et al., *Mitochondrial Phosphoenolpyruvate Carboxykinase Regulates Metabolic Adaptation and Enables Glucose-Independent Tumor Growth.* Mol Cell, 2015. **60**(2): p. 195-207.
30. van der Reest, J., et al., *Proteome-wide analysis of cysteine oxidation reveals metabolic sensitivity to redox stress.* Nature Communications, 2018. **9**(1): p. 1581.
31. Yang, C., et al., *Glutamine oxidation maintains the TCA cycle and cell survival during impaired mitochondrial pyruvate transport.* Mol Cell, 2014. **56**(3): p. 414-424.
32. Lyssiotis, C.A. and A.C. Kimmelman, *Metabolic Interactions in the Tumor Microenvironment.* Trends in Cell Biology, 2017. **27**(11): p. 863-875.
33. Hui, S., et al., *Glucose feeds the TCA cycle via circulating lactate.* Nature, 2017. **551**(7678): p. 115-118.
34. Faubert, B., et al., *Lactate Metabolism in Human Lung Tumors.* Cell, 2017. **171**(2): p. 358-371.e9.
35. Cheung, S.M., et al., *Lactate concentration in breast cancer using advanced magnetic resonance spectroscopy.* British Journal of Cancer, 2020. **123**(2): p. 261-267.
36. Leithner, K., et al., *The glycerol backbone of phospholipids derives from noncarbohydrate precursors in starved lung cancer cells.* Proceedings of the National Academy of Sciences, 2018. **115**(24): p. 6225-6230.
37. Buescher, J.M., et al., *A roadmap for interpreting (13)C metabolite labeling patterns from cells.* Curr Opin Biotechnol, 2015. **34**: p. 189-201.
38. Vande Voorde, J., et al., *Improving the metabolic fidelity of cancer models with a physiological cell culture medium.* Sci Adv, 2019. **5**(1): p. eaau7314.
39. Lemaigre, F.P. and G.G. Rousseau, *Transcriptional control of genes that regulate glycolysis and gluconeogenesis in adult liver.* Biochem J, 1994. **303 (Pt 1)**(Pt 1): p. 1-14.
40. Kano, A., T. Iwasaki, and M. Shindo, *Bongkrekic acid facilitates glycolysis in cultured cells and induces cell death under low glucose conditions.* Biochemistry and Biophysics Reports, 2019. **20**: p. 100683.
41. Anastasiou, D., et al., *Pyruvate kinase M2 activators promote tetramer formation and suppress tumorigenesis.* Nat Chem Biol, 2012. **8**(10): p. 839-47.
42. Dayton, T.L., T. Jacks, and M.G. Vander Heiden, *PKM2, cancer metabolism, and the road ahead.* EMBO Rep, 2016. **17**(12): p. 1721-1730.
43. Dombrauckas, J.D., B.D. Santarsiero, and A.D. Mesecar, *Structural basis for tumor pyruvate kinase M2 allosteric regulation and catalysis.* Biochemistry, 2005. **44**(27): p. 9417-29.
44. Weinstabl, H., et al., *Intracellular Trapping of the Selective Phosphoglycerate Dehydrogenase (PHGDH) Inhibitor BI-4924 Disrupts Serine Biosynthesis.* J Med Chem, 2019. **62**(17): p. 7976-7997.
45. Smith, G.K., et al., *Activity of an NAD-dependent 5,10-methylenetetrahydrofolate dehydrogenase in normal tissue, neoplastic cells, and oncogene-transformed cells.* Arch Biochem Biophys, 1990. **283**(2): p. 367-71.
46. Lorenz, N.I., et al., *AMP-kinase mediates adaptation of glioblastoma cells to conditions of the tumour microenvironment.* bioRxiv, 2022: p. 2022.03.25.485624.
47. Fan, J., et al., *Quantitative flux analysis reveals folate-dependent NADPH production.* Nature, 2014. **510**(7504): p. 298-302.
48. Bichi, R., et al., *Human chronic lymphocytic leukemia modeled in mouse by targeted TCL1 expression.* Proc Natl Acad Sci U S A, 2002. **99**(10): p. 6955-60.
49. Chakraborty, S., et al., *B-cell receptor signaling and genetic lesions in TP53 and CDKN2A/CDKN2B cooperate in Richter transformation.* Blood, 2021. **138**(12): p. 1053-1066.
50. Nelson, D.L.a., *Lehninger principles of biochemistry*. 2017, New York, NY, USA: W.H. Freeman and Company ; Houndmills, Basingstoke : Macmillan Higher Education.

51. Chaneton, B., et al., *Serine is a natural ligand and allosteric activator of pyruvate kinase M2.* Nature, 2012. **491**(7424): p. 458-462.
52. Ye, J., et al., *Pyruvate kinase M2 promotes de novo serine synthesis to sustain mTORC1 activity and cell proliferation.* Proceedings of the National Academy of Sciences, 2012. **109**(18): p. 6904-6909.
53. Rossi, M., et al., *PHGDH heterogeneity potentiates cancer cell dissemination and metastasis.* Nature, 2022. **605**(7911): p. 747-753.
54. Muir, A. and M.G. Vander Heiden, *The nutrient environment affects therapy.* Science, 2018. **360**(6392): p. 962-963.
55. Zheng, Y., et al., *Mitochondrial One-Carbon Pathway Supports Cytosolic Folate Integrity in Cancer Cells.* Cell, 2018. **175**(6): p. 1546-1560.e17.
56. Kiweler, N., et al., *Mitochondria preserve an autarkic one-carbon cycle to confer growth-independent cancer cell migration and metastasis.* Nat Commun, 2022. **13**(1): p. 2699.
57. Hiller, K., et al., *MetaboliteDetector: comprehensive analysis tool for targeted and nontargeted GC/MS based metabolome analysis.* Anal Chem, 2009. **81**(9): p. 3429-39.
58. Wang, T., et al., *Inosine is an alternative carbon source for CD8(+)-T-cell function under glucose restriction.* Nat Metab, 2020. **2**(7): p. 635-647.
59. Dranka, B.P., et al., *Assessing bioenergetic function in response to oxidative stress by metabolic profiling.* Free Radic Biol Med, 2011. **51**(9): p. 1621-35.